

## ELECTRONIC SUPPLEMENTARY INFORMATION (ESI)

### Dynamic sampling in autonomous process optimization

Melodie Christensen,<sup>a,b\*</sup> Yuting Xu,<sup>b</sup> Eugene Kwan,<sup>b</sup> Michael J. Di Maso,<sup>b</sup> Yining Ji,<sup>b</sup> Mikhail Reibarkh,<sup>b</sup> Alexandra Sun,<sup>b</sup> Andy Liaw,<sup>b</sup> Patrick Fier,<sup>b</sup> Shane Grosser,<sup>b</sup> and Jason E. Hein.<sup>a,c,d\*</sup>

*a. Department of Chemistry, University of British Columbia, Vancouver, British Columbia V6T 1Z1, Canada.*

*b. Department of Process Research and Development, Merck & Co., Inc., Rahway, NJ 07065, United States.*

*c. Acceleration Consortium, University of Toronto, Toronto, ON, Canada*

*d. Department of Chemistry, University of Bergen, Bergen, Norway*

*† Correspondence: [melodie.christensen@merck.com](mailto:melodie.christensen@merck.com); [jhein@chem.ubc.ca](mailto:jhein@chem.ubc.ca)*

# Contents

<b>ESI.1. High-throughput reaction profiling with DBDMH .....</b>	<b>3</b>
<b>ESI.2. Photoreactor development .....</b>	<b>4</b>
<b>ESI.3. Plateau detection algorithm selection .....</b>	<b>6</b>
<b>ESI.4. Optimization algorithm selection .....</b>	<b>7</b>
<b>ESI.5. Closed-loop integration of the autonomous optimizer components .....</b>	<b>10</b>
<b>ESI.6. Reproducibility assessment .....</b>	<b>11</b>
<b>ESI.7. Scale-up studies.....</b>	<b>12</b>
<b>ESI.8. Optimization performance assessment.....</b>	<b>13</b>
<b>ESI.9. NMR Studies to the interaction of reaction components prior to irradiation .....</b>	<b>17</b>
<b>ESI.10. Analysis of random forest parameter importance modeling.....</b>	<b>19</b>
<b>ESI.11. Experimental.....</b>	<b>22</b>
<b>ESI.12. Characterization data .....</b>	<b>28</b>
<b>ESI.13. Analytical methods .....</b>	<b>32</b>
<b>ESI.14. Chemspeed protocol .....</b>	<b>33</b>
<b>ESI References .....</b>	<b>35</b>

## ESI.1. High-throughput reaction profiling with DBDMH

In high-throughput reaction profiling studies, poor reactivity was observed with DBDMH, even in the presence of acid additive (Figure SI.1).

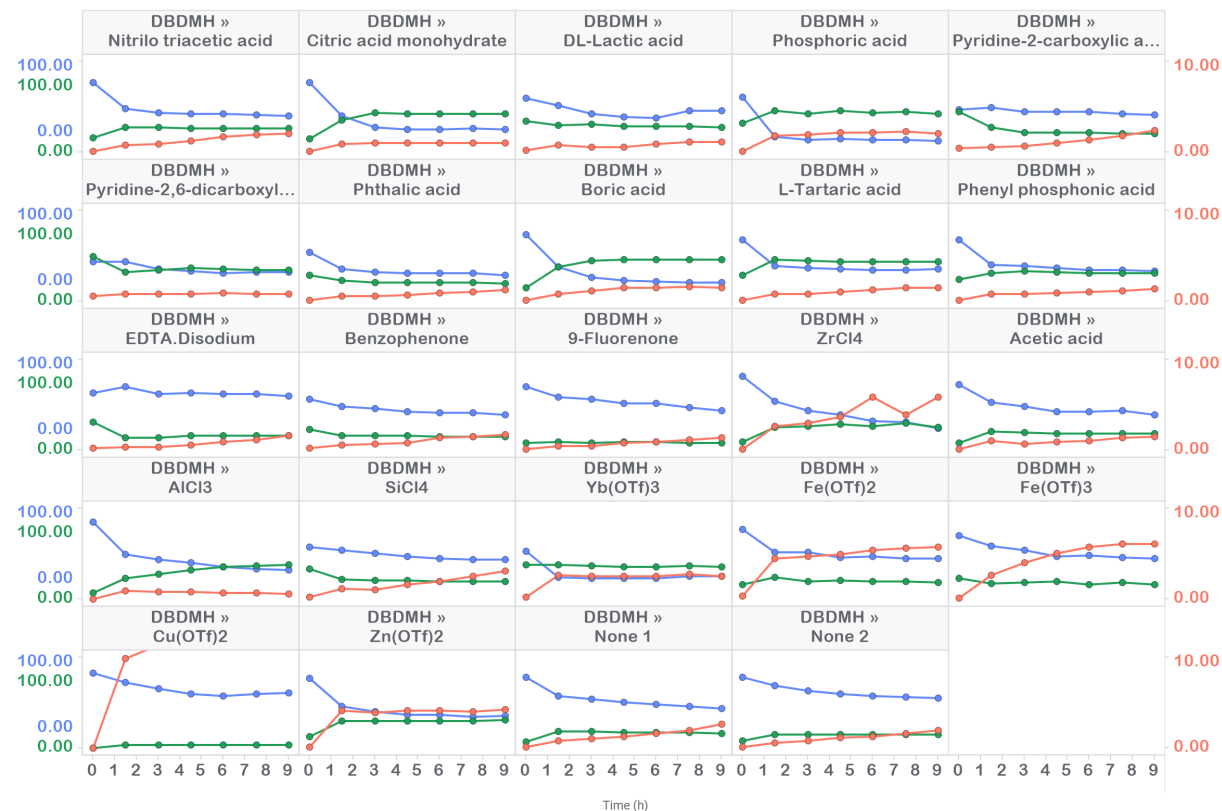


**Figure SI.1.** High-throughput reaction profiling evaluating DBDMH in the presence of 22 acid additives, along with replicate additive-free conditions

UPLC area % of starting material **1** (blue), product **2** (green) and side product **3** (red) measured over 9 hours in 1.5 hour time intervals.

Conditions: 63  $\mu\text{mol}$  **1**, 69.3  $\mu\text{mol}$  DBDMH and 6.3  $\mu\text{mol}$  acid additive in ACN (0.25M) irradiated with 405 nm LEDs at 60 mW (level 1) intensity for 9 h at 10 - 30  $^{\circ}\text{C}$ .

## ESI.2. Photoreactor development

Photons are a reagent in photochemical transformations, thus, effective and robust photon delivery is a critical aspect of automated photochemical reaction execution. Popular systems for batch photochemistry include the Penn PhD system,<sup>1</sup> which can accommodate one millimole-scale reaction, as well as the SynLED and TAK-120 systems, which can accommodate up to ten millimole-scale reactions.<sup>2</sup> When it comes to miniaturized, high-throughput batch photoreactor systems, the Lumidox photoreactor systems from Analytical Sales has seen widespread implementation in the photochemistry field.<sup>3</sup> Here, up to 96 micromole-scale reactions can be executed in parallel, with one LED dedicated to each reaction well. The Lumidox LED panels, coupled with glass-bottomed 96-well Paradox photoreactors, have been reported in a number of high-throughput photochemistry optimizations.<sup>4,5</sup> Two generations of the Lumidox LED panels exist, with the Lumidox II panels offering higher light intensities than the less powerful Lumidox I panels. Due to the wide range of LED light wavelengths and intensities available with the Lumidox II panels, we selected these for evaluation and characterization.

The parameters we were interested in characterizing were efficient photon delivery with uniform temperature control. We were aware that Lumidox II LED panels could lead to well temperature increases up to 25 °C at the lowest light intensity, and therefore initiated our studies at level 1 light intensity (60 mW per well). We implemented a temperature feedback loop to maintain the photoreactor temperature at 25 °C through active cooling of the base of the LED array with a chiller-cooled circulator block. We monitored the photoreactor temperature with the LED panel on for 60 minutes, then off for 60 minutes, and repeated this cycle six times. Upon switching the LED array on, the photoreactor temperature increased to 33 °C, and upon switching the LED array off, the photoreactor temperature decreased to 10 °C (Figure SI.2). We attributed these temperature swings to ineffective cooling of the photoreactor, as the chiller-cooled circulator block was only in contact with the base of the LED panel.

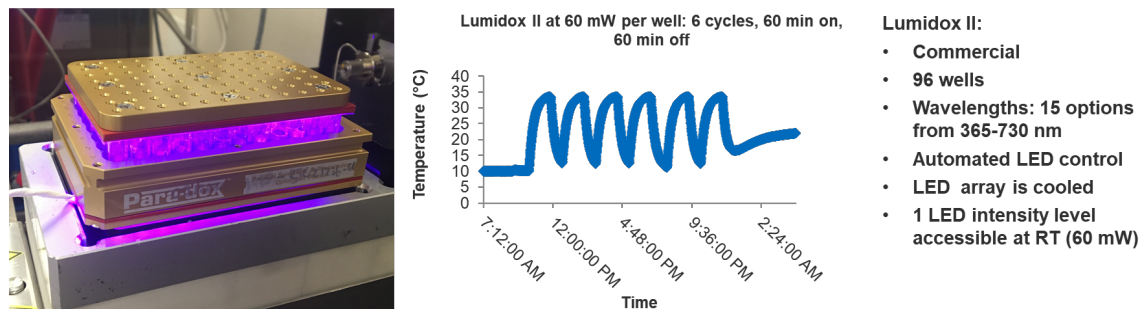


**Figure SI.2.** Temperature monitoring of the Lumidox II LED panel with the Paradox photoreactor

We therefore turned to Analytical Sales for the development of a more efficiently cooled photoreactor system that could access all five light intensities (60-385 mW) while maintaining a photoreactor temperature of 25 °C. Analytical Sales moved forward with the design and prototyped a custom photoreactor with cooling channels incorporated between the rows of wells. In order to accommodate these cooling channels, the number of wells were decreased from 96 to 48. The custom photoreactor was aptly named the temperature-controlled reactor (TCR). We implemented a temperature feedback loop to maintain the TCR temperature at 25 °C. Here, in addition to active cooling of the base of the LED array with a chiller-cooled circulator block, a tubing connection was established to flow the chiller fluid through the TCR cooling channels. We monitored the photoreactor temperature with the LED panel on for 30 minutes, then off for 30 minutes, at each light intensity level from 60 mW per well through 385 mW per well. With the implementation of the TCR cooling channels, excellent temperature control was achieved across all five light intensity levels, and the temperature was maintained between 24 and 26 °C, measured at three well positions (Figure SI.3). With these results in hand, we integrated the Lumidox TCR LED controller, the Huber circulating chiller and a V&P scientific tumble stirrer through RS232 connections to enable the direct Chemspeed Autosuite software control of illumination, cooling and stirring. With this, we were ready to optimize photochemical reactions in high throughput.

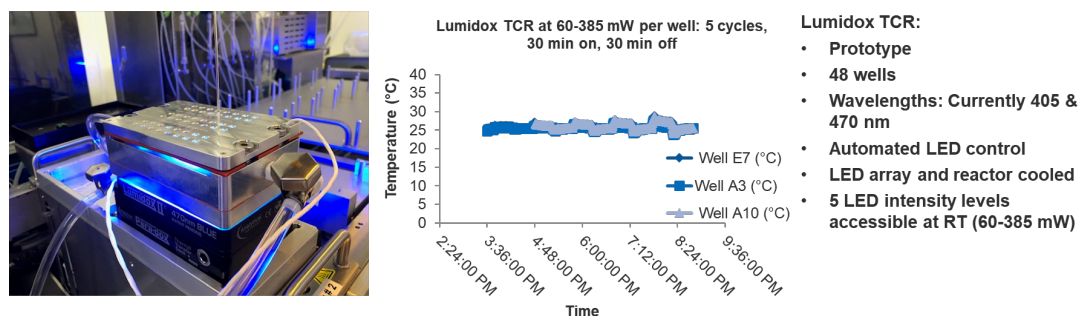


**Figure SI.3.** Temperature monitoring of the Lumidox TCR photoreactor

### ESI.3. Plateau detection algorithm selection

The next challenge was to develop an effective real time plateau detection method based on the following assumptions: (1) the experimental outcome  $Y(t)$  is measured sequentially at different timepoints  $t=(t_0, t_1, t_2, \dots)$ , (2) the experimental outcome at each timepoint is denoted as  $Y=(Y_0, Y_1, Y_2, \dots)$ , (3) the experimental conditions are denoted as  $X=(X_1, X_2, X_3, \dots)$ , (4) the goal of real time plateau detection is that at any time  $t$ , given the experimental conditions  $X$ , and all previous measurements  $\{Y(s)\}_{s < t}$ , to decide whether the experiment has reached a “plateau” and can be stopped. Given these assumptions, three real time plateau detection methods were evaluated against existing data.

Algorithm 1 (maximum negative difference): The maximum negative difference approach assumes that after reaching a plateau, there are still fluctuations across time, assuming the maximum negative difference of  $Y(t)$  is caused by random fluctuations. The experiment reaches a plateau at  $t$  if  $|Y_t - Y_{t-1}| \leq \delta$ , where the threshold is computed from previous data by:  $\delta = \max_{\{Y_s < Y_{s-1}\}} \{|Y_s - Y_{s-1}|\}$ .

Algorithm 2 (plateau variability): The plateau variability approach assumes that after reaching plateau, assuming  $Y_t \sim N(\mu, \sigma^2)$ , then  $\delta Y = Y_t - Y_{t-1} \sim N(0, 2 * \sigma^2)$ . The 95% confidence interval of  $\delta Y$  is:  $\pm 1.96 * \sqrt{2} * \sigma$ . The experiment reaches plateau at  $t-1$  if  $|Y_t - Y_{t-1}| \leq \delta$ , where the threshold is computed from previous data by:  $\delta = 1.96 * \sqrt{2} * \sigma$ . The parameters  $(\mu, \sigma)$  can also be estimated from previous data.

Algorithm 3 (threshold of slope): The threshold of slope approach assumes that the slope at time  $t$  is  $s(t) = (Y_t - Y_{t-1}) / \Delta t$ ; ( $t \geq 2$ ), where  $\Delta t$  is the time interval. The experiment reaches plateau at  $t$  if the slope is less than a certain threshold:  $s(t) \leq \delta$ , where the dynamic threshold is based on only previous data under the same conditions:  $\delta(t) = 0.3 * 1 / (t-2) \sum_{i=2}^{t-1} s(i)$ .

Of the three approaches, algorithm 2 performed optimally. Upon manually validating the automated plateau labeling of a set of historically captured reaction profiles, 170 out of 184 of plateaus were labeled correctly (the failures included 1 false negatives, 9 false positives and 4 time adjustments. Figure SI.4). This corresponded to a success rate of 92%. Thus, real time plateau detection algorithm 2 was implemented for use in real-time autonomous plateau detection.

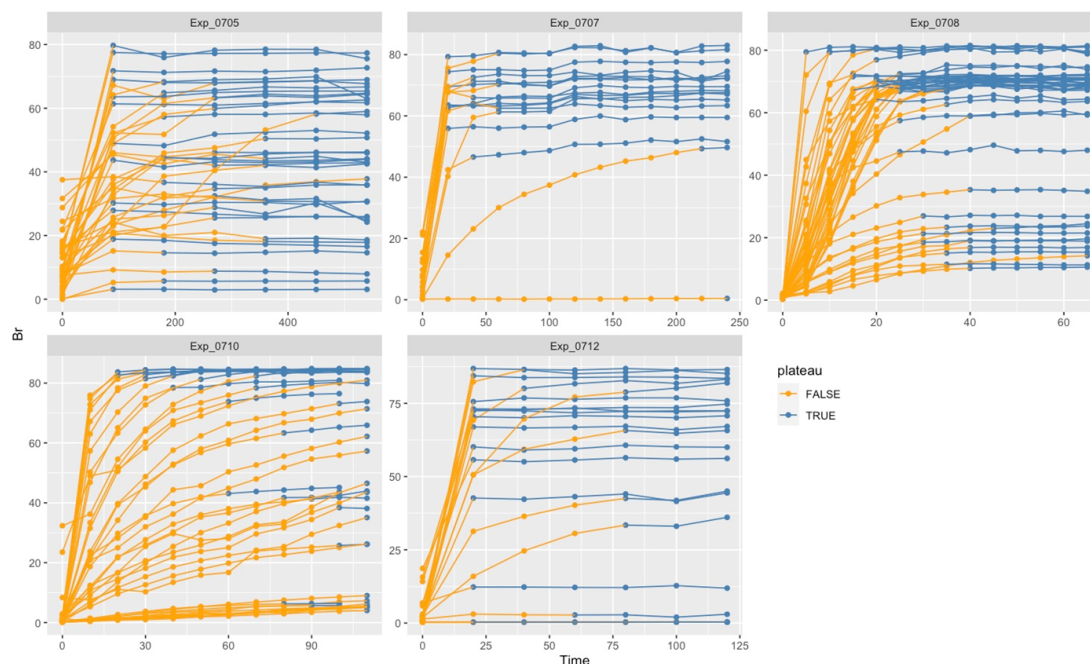


**Figure SI.4.** Evaluation of the algorithm 2 on historically captured reaction profile data

#### ESI.4. Optimization algorithm selection

The next step in building an autonomous optimizer for photochemical reactions was the definition of a sequential model based optimization strategy. Sequential model based optimization strategies rely upon the construction of a surrogate model of the objective function for the defined parameter space.<sup>6</sup> The modeling is necessary because the objective function is typically not known, complex or difficult to sample in chemical process optimizations. Thus, a statistical surrogate model is constructed from a set of seed experiments, and an acquisition function is utilized to propose new experiments, the results of which feed into improving the surrogate model, from which the acquisition function proposes new experiments. This cycle is continued until a predefined output parameter threshold or number of experiments is reached (Figure SI.5). Here we discuss the selection of algorithms for each step in this workflow. A significant portion of our code draws from open-source Python libraries.<sup>7</sup>

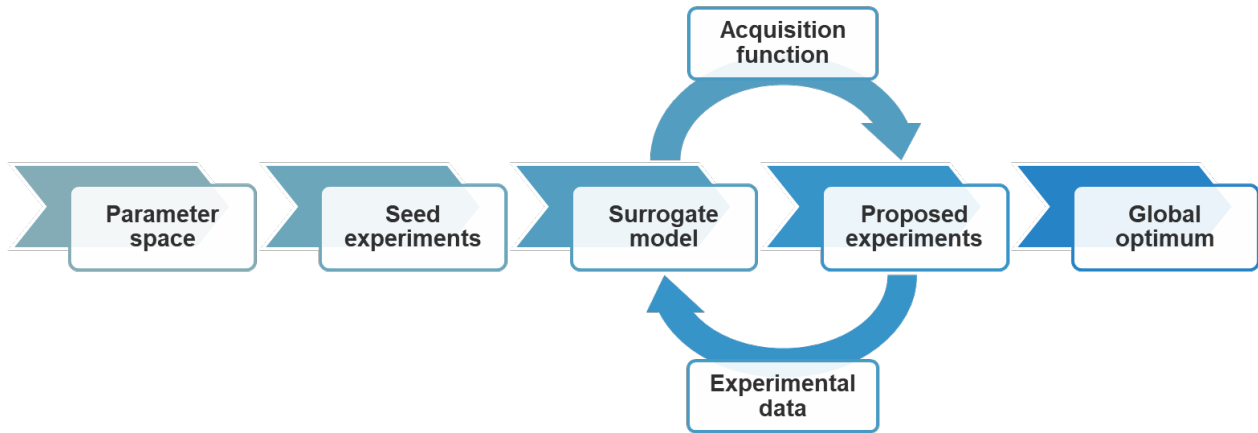


**Figure SI.5.** Steps in a sequential model based optimization workflow

The first decision point was the threshold for optimization. Here, 48 experiments were selected as the maximum threshold. The first eight of these experiments were designated as seed experiments, and the subsequent 40 were dedicated to optimization. With respect to the seed experiments, as opposed to random sampling of the parameter space, a D-optimal design was utilized to seed the parameter space more uniformly.<sup>8</sup> The second decision point was the modeling strategy for constructing the statistical approximation of the objective function. Linear regression modeling was deemed a plausible approach, but so was Gaussian process modeling. Instead of opting for a single modeling method, a more pragmatic approach employing both modeling methods was pursued. Also, if the model failed to predict a better experimental proposal, the selection strategy would revert to random sampling, allowing the model to be updated with additional data. The third decision point was the acquisition function. For linear regression modeling, the options included the predicted mean, prediction with standard error and upper prediction interval (UPR). Because each of these functions performed similarly in simulations, the predicted mean acquisition method was selected for linear regression modeling.<sup>9</sup> For Bayesian optimization (BO) through Gaussian process modeling, the options to choose from included expected improvement (EI), probability of improvement (PI) and upper confidence bound (UCB).<sup>10,11</sup> Again, because each of these functions performed similarly in simulations, expected improvement was selected for the first autonomous experiment (Figure SI.6). However, in later experiments, the selection was widened to include all three BO acquisition functions.

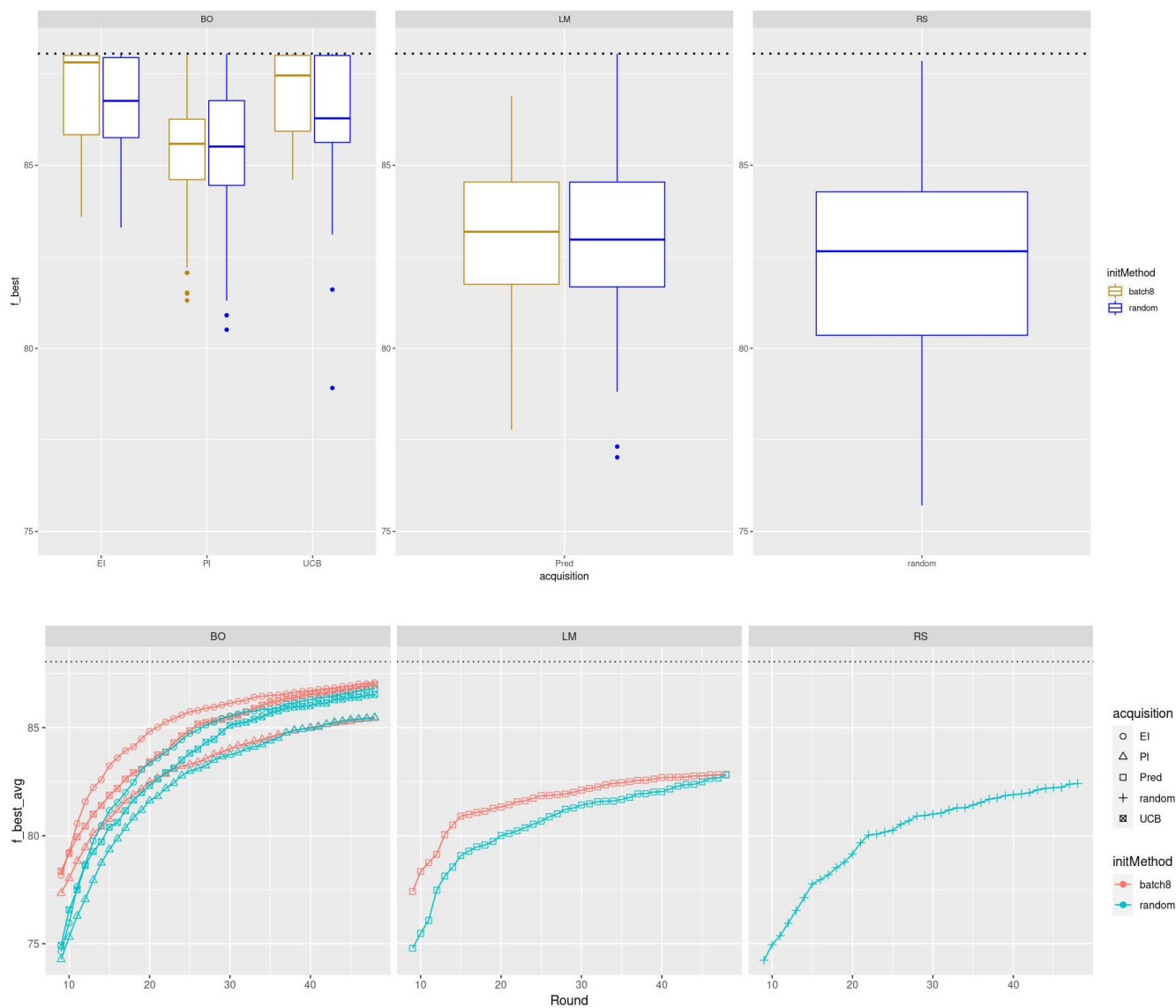


**Figure SI.6.** Simulated optimization runs based on a neural network model of historically captured reaction profile data  
 Each simulated optimization was repeated 100 times.

### ESI.5. Closed-loop integration of the autonomous optimizer components

The final step in rendering the system autonomous was the development of a data integration strategy among the hardware and software components (Figure SI.7). For this, a Python interface was developed to configure the input parameters and ranges, input stock mixture concentrations, output parameters, UPLC retention times, retention time windows, and file locations. The optimizer code was configured to suggest an experiments based on the configured parameters. Once the optimizer code suggested an experiment, the interface code was designed to translate this to dispense volumes for experimental execution by the Chemspeed Autosuite software, which was programmed to monitor the dispense volume file for new entries. Once the experimental execution was completed, a sample aliquot was injected into the sample valve. This was followed by a digital relay switch to trigger UPLC acquisition through the Agilent Chemstation software. Upon UPLC data processing via the Chemstation software, an auto-generated results file was parsed by the interface code, and the output relayed to the optimizer code, where the plateau detection algorithm determined whether or not a plateau had been reached. If the plateau was not reached, the interface software triggered the Chemspeed Autosuite software to aliquot additional samples. Once the plateau was reached, the interface triggered the Chemspeed software to terminate sampling, and relayed the final experimental results to the optimizer code, which then suggested the next experiment through a pre-configured sequential-model based optimization algorithm (linear model based or Gaussian process model based BO). The Python code and autonomous optimization data sets can be accessed publicly at <https://github.com/ekwan/zhulong.git> .

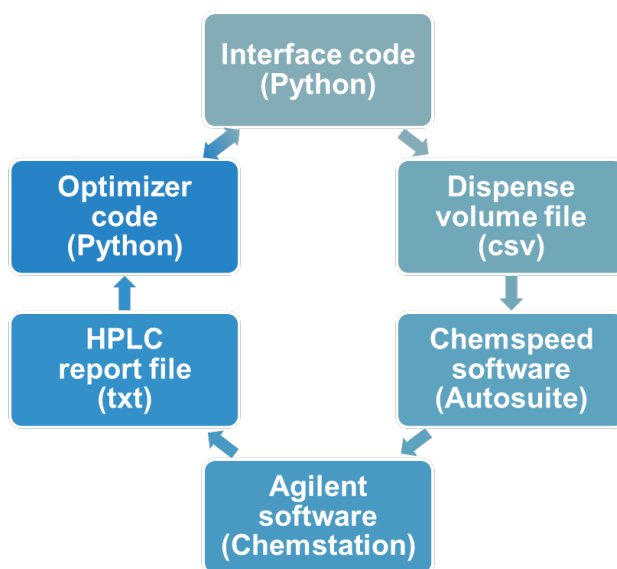


**Figure SI.7.** Data flow in the integrated closed-loop optimization system

## ESI.6. Reproducibility assessment

Reproducibility experiments are useful in the development of autonomous systems because they have the potential to uncover both hardware and software issues, but more importantly, provide researchers with the confidence to trust self-optimization results. Our system posed an extra level of challenge in that a demonstration of consistent and reliable reaction profiles under constant reaction conditions were a requirement.

Four reproducibility runs were carried out, and different hardware and software issues were resolved with each run until excellent reproducibility was observed in run 4 (Table SI.1 and Figure SI.8). In the first run, the stock solution concentrations were high, which led to several to exist as solid liquid slurries. Although the wide bore Chemspeed needles, with their 0.8 mm inner diameters, are capable of slurry transfers, the accuracy and precision of the transfers suffered. Thus, in the first run, the reproducibility was extremely poor, where different reaction rates were observed in experiments carried out under the same conditions in two solvents, ACN and DMC. The stock mixture concentrations were gradually reduced until the compounds were fully dissolved, improving the process performance until excellent reproducibility was observed in runs 3 and 4. The reduction in stock solution concentrations resulted in a reduction of the reaction concentration, which increased the reaction rate under the same light intensity.

**Table SI.1.** Stock solution concentrations for reproducibility testing

	Run 1	Run 2	Run 3	Run 4
<b>Scale in 4</b>	63 $\mu$ mol	25 $\mu$ mol	20 $\mu$ mol	20 $\mu$ mol
<b>[1] stock</b>	0.630 M	0.250 M	0.250 M	0.250 M
<b>[NBS] stock</b>	0.945 M	0.375 M	0.250 M	0.250 M
<b>[H<sub>2</sub>SO<sub>4</sub>] stock</b>	0.315 M	0.125 M	0.100 M	0.100 M
<b>[3.1] reaction</b>	0.252 M	0.100 M	0.080 M	0.080 M
<b>Temperature</b>	25 °C	25 °C	25 °C	5 °C
<b>Wavelength</b>	470 nm	470 nm	470 nm	405 nm*

\*470 nm LED array that warped due to incompatibility with Syltherm at high temperature was replaced with a 405 nm LED array. Green: Slurry in ACN and DMC; Blue: slurry in DMC.



was determined to be minimal on a large scale as well. 1.5 g of pyridazinone **1** was passed through a Vaportec 3 ml reactor with a flow rate of 0.5 ml/min for 65 min at 10 °C to generate product **2** in 69% assay yield and product **3** in 13% assay yield, with 5% starting material **1** remaining, thus, the mass balance was determined to be 87% (Figure SI.9). Reaction profiles were similar to those observed on micromole-scale in batch. This experiment confirmed that micromole-scale results in batch could be translated to millimole-scale in flow.

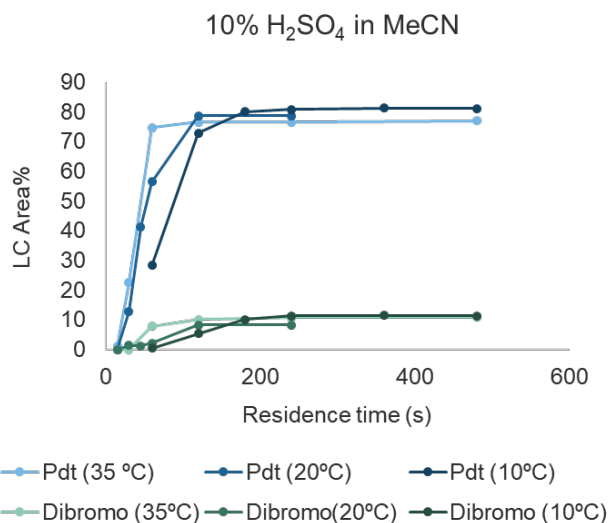
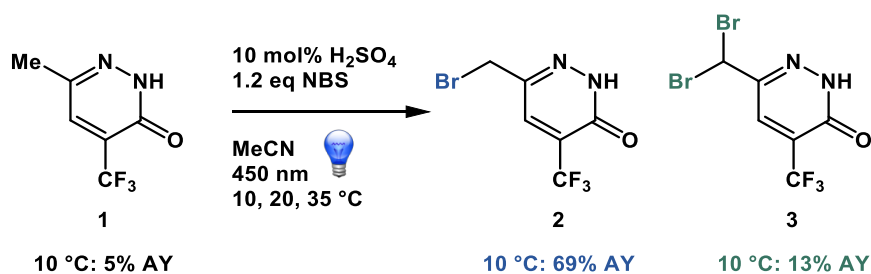


**Figure SI.9. Scale-up experiments in a Vaportec photoreactor.**

### ESI.8. Optimization performance assessment

An important question to answer in researching optimization algorithms for chemical process optimization is how well the technology performs with respect to (1) arrival at a global optimum, and (2) gaining process insights. The parameter space in this optimization certainly proved to be challenging, with several local optima of similar performance as well as

interactions among the various parameters. Since we employed three different optimization approaches, we reasoned that comparisons of these three approaches did provide us with a better understanding around the influence of the model choice and sampling strategy on the optimization performance. Firstly, our linear model assumed a linear relationship between the additive loading and the product level at reaction plateau, while allowing for nonlinear relationships with the rest of the numerical variables. Thus, the regressors in our 'linear model' approach contained a linear term for the additive loading as well as quadratic terms for all the other numerical input variables (additive pKa, temperature, stage, reagent equivalents). This assumption was proven incorrect in the first optimization run, where we found that high loadings of low pKa acids resulted in low levels of product. This incorrect assumption was based on the high throughput reaction profiling data, but we had not explored as wide of a range of additive loadings in those experiments. Thus, even the most informed assumptions made in developing regression models may lead to poor optimization performance, if incorrect. Bayesian optimization, on the other hand, is based on GP model approximations of the seed data and thus is not tied to such assumptions. Therefore, BO through GP regression would be our first choice in future optimizations.

The impact of the sampling strategy on optimization performance was also explored. Figure SI.10 illustrates box plots of the medians and interquartile ranges of product LC area % upon the implementation of different acquisition functions for sampling the parameter space. The literature indicated that PI would be the most exploitative acquisition function, sampling closer to the predicted optimum, and that UCB would be the most explorative acquisition function, sampling areas of high uncertainty.<sup>10,11</sup> The data illustrated in the box plots support this literature precedent. For example, in run 3, where the EI, PI and UCB strategies were alternated in the same run, PI sampled areas that produced product levels close to the optimum (exploitation), while UCB sampled areas that produced a wider range of product levels (exploration). Intuitively, one might speculate that sampling closer to the predicted optimum to be more effective, but when faced with objective functions with multiple local optima, some exploration is critical to determination of the global optimum.

Another way to compare the various sampling strategies was to compare the number of iterations dedicated to each additive using each acquisition function (Figure SI.11). As expected, in the third Bayesian optimization run, UCB sampled 7 out of 8 additives, while PI focused on 3, and EI sampled 5. In the second Bayesian optimization run, EI once again sampled 5 out of 8 additives. Finally, in the first LM based optimization run, mean best prediction sampled 5 out of 8 additives.

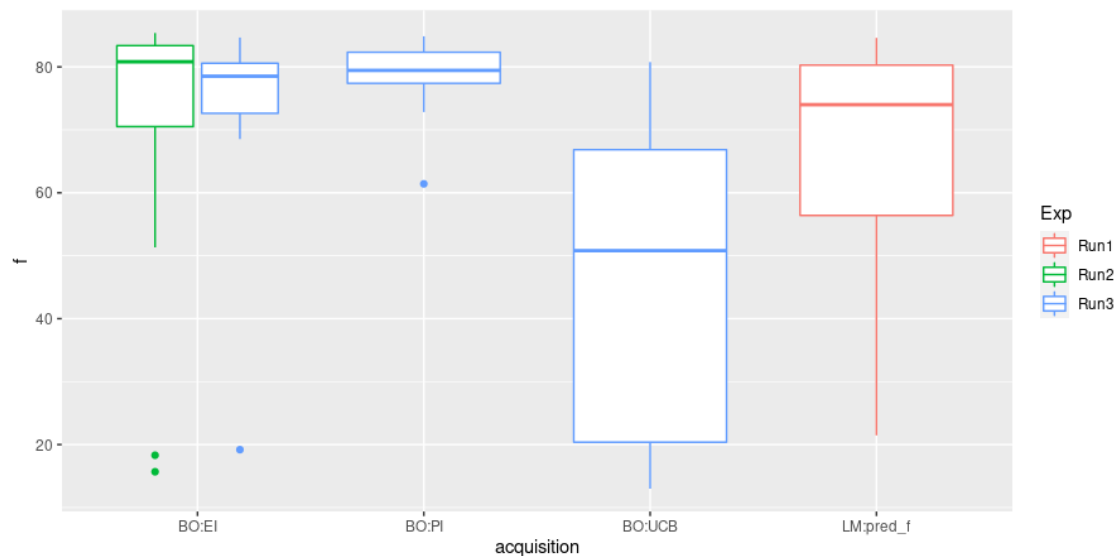


**Figure SI.10.** Box plot of LC area % product under various sampling strategies

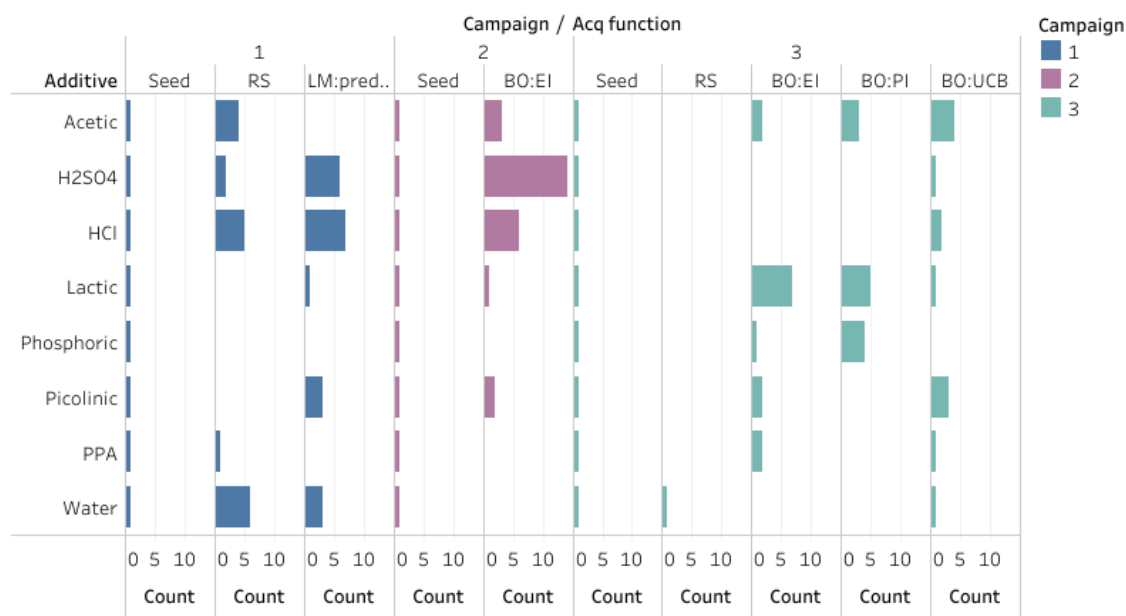


**Figure SI.11.** Count of iterations per each additive under different sampling strategies

Finally, we were interested in understanding both the convergence behavior and sampling diversity of each optimization strategy. We turned to multidimensional scaling (MDS) in order to flatten the combinatorial parameter space and more clearly observe the optimization trajectory (Figure SI.12).<sup>13</sup> This allowed for (1) the establishment of evidence for optimization convergence and (2) the assessment of diversity in sampling the combinatorial parameter space. As mentioned previously, the goal of the optimization was to achieve a balance between

a global optimum while gaining sufficient insight into the process robustness. Figure SI.12.a indicates that runs 2 and 3 converged, but run 1 did not. Figure SI.12.b. indicates that the highest sampling diversity was observed in run 1, but the diversity was attributed to random sampling upon the inability of the linear regression model to make better predictions. The sampling diversity was moderately high in run 3 due to the implementation of three different acquisition functions. Interestingly, it appears that the optimizer was sampling in circles at one point in the run 3 as it cycled between the three acquisition functions, thus, in future optimizations, it may be more effective to begin with UCB in order to increase the initial sampling diversity, then switch to EI in the second half of the run to facilitate convergence.

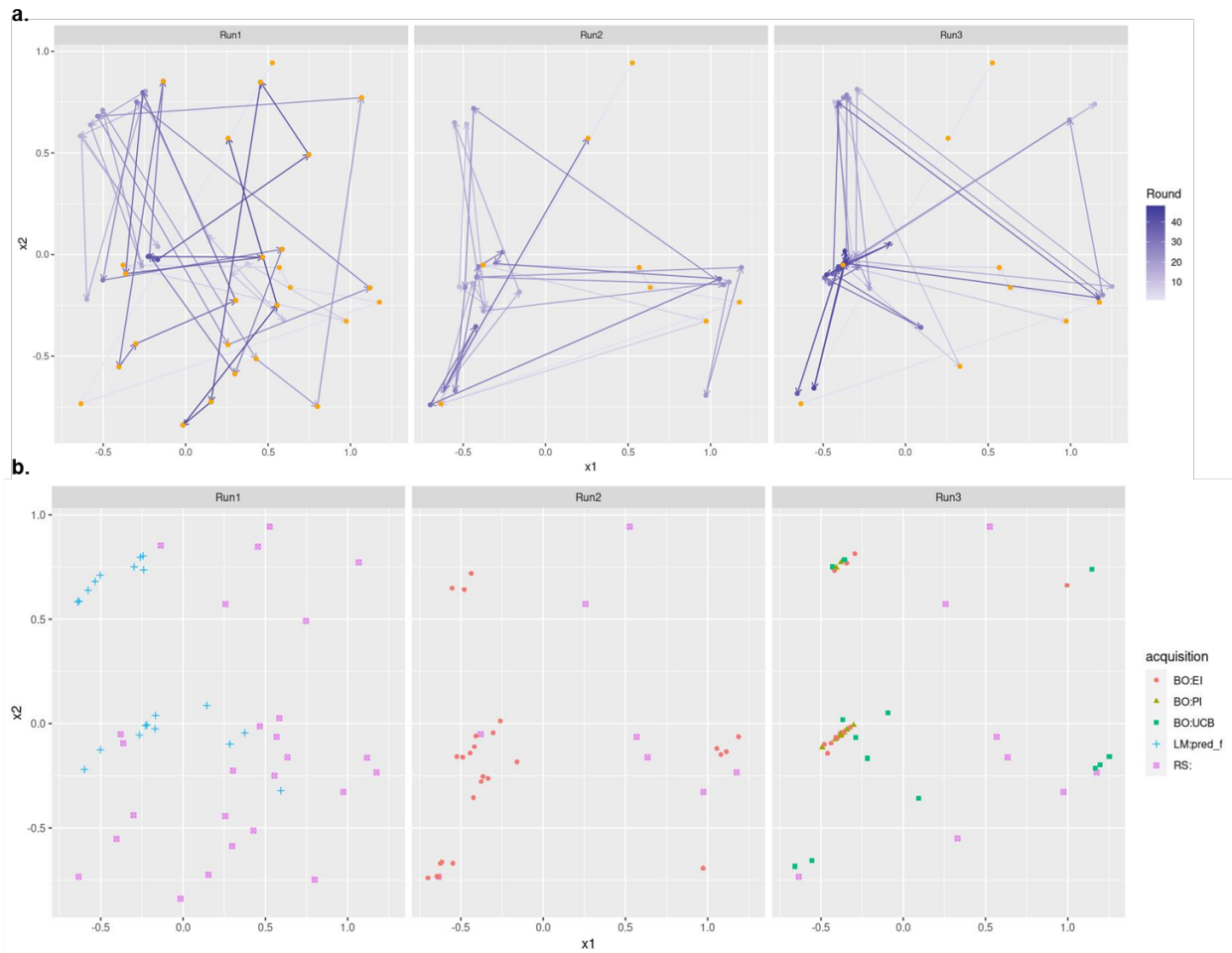


**Figure SI.12.** Multidimensional scaling (MDS) visualizations

a) The optimization trajectory in three runs, with the purple arrows illustrating the optimization path (from light to dark) and yellow points indicating the initial seed and random samples. b) The sampling diversity colored by the different acquisition functions implemented in each strategy.

## ESI.9. NMR Studies to the interaction of reaction components prior to irradiation

NMR studies were performed to understand the impact of various reaction species on NBS.

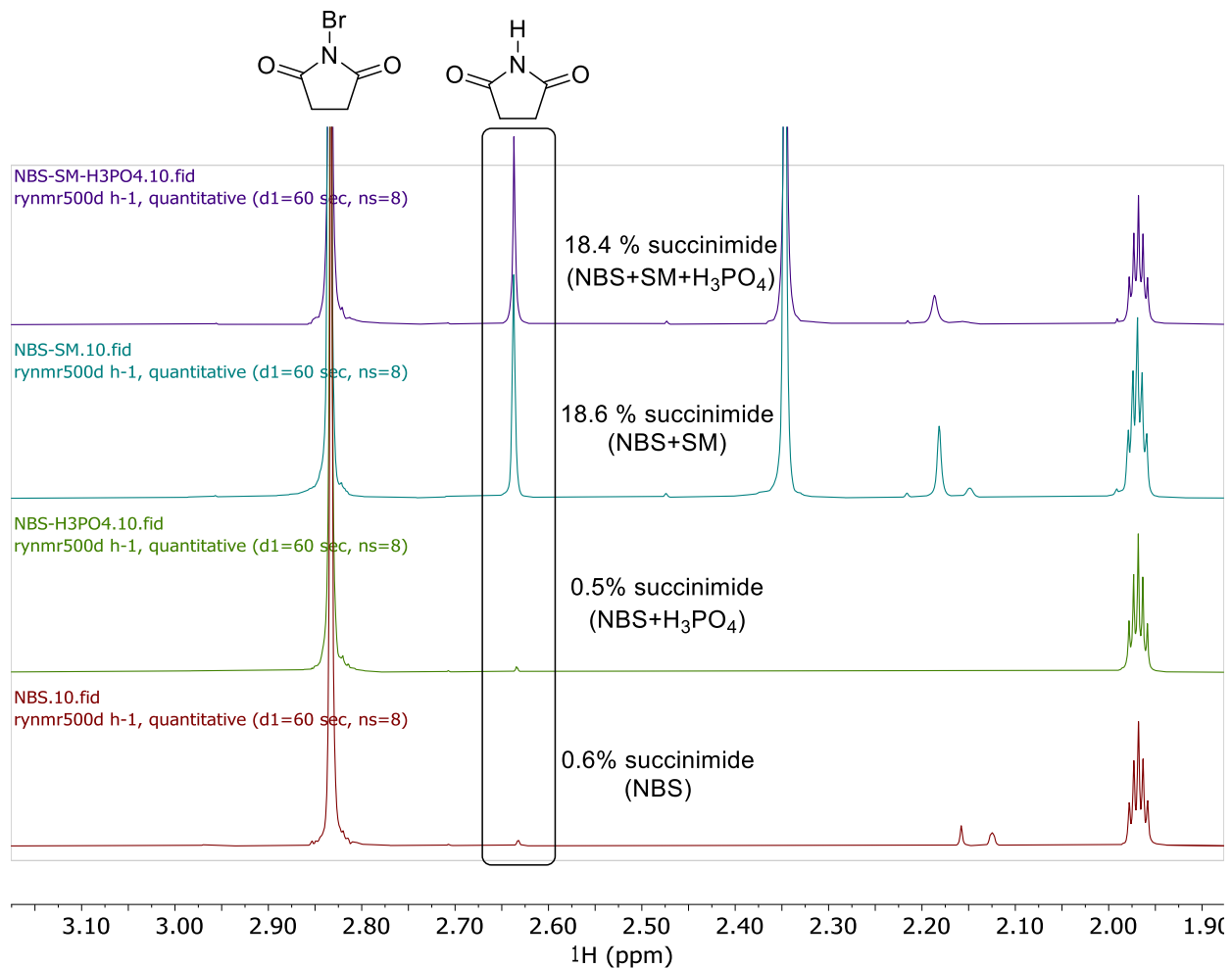


**Figure SI.13.** NMR studies of NBS with the addition of various reaction species in solution

NMR studies were performed to understand the equilibrium between pyridazinone **1** and succinimide.

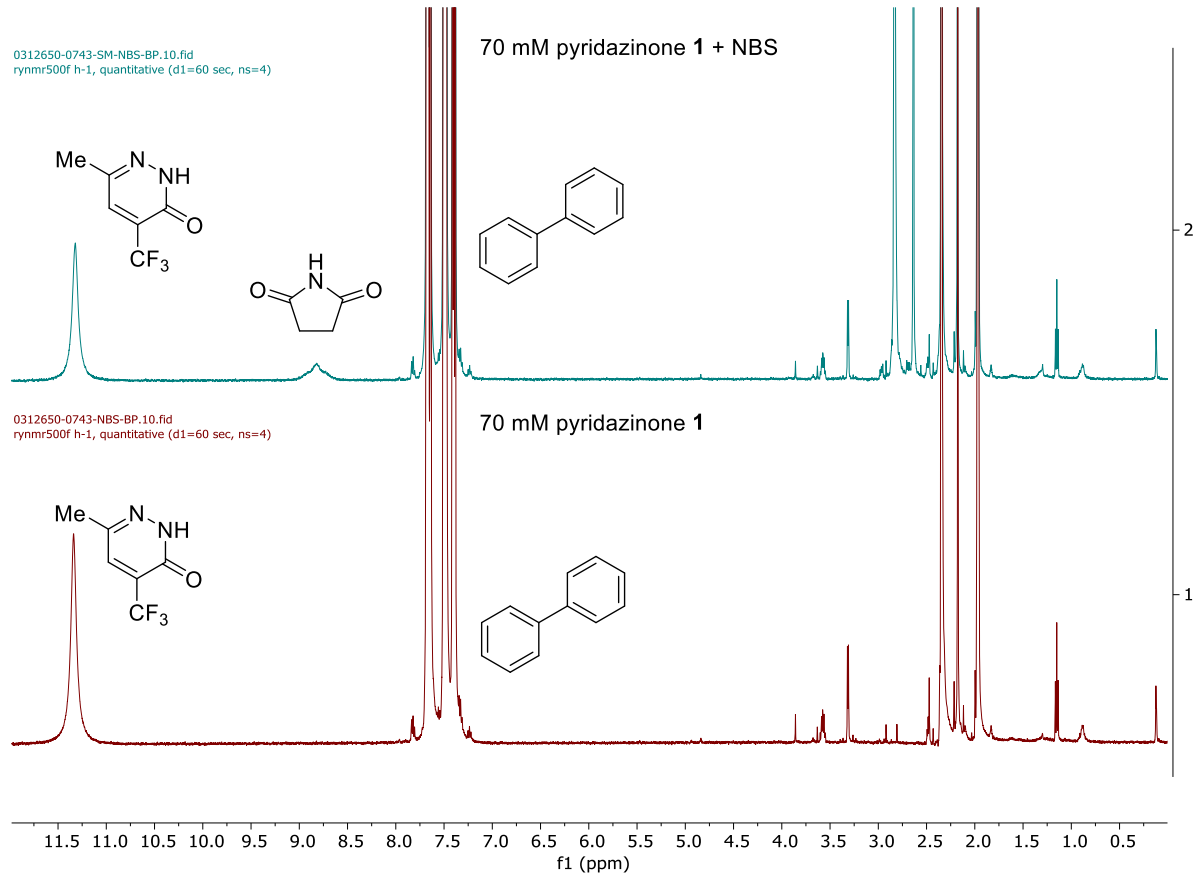


**Figure SI.14.** NMR studies of pyridazinone **1** and NBS

**Table SI.2.** Assays to determine pyridazinone **1** and succinimide concentrations

<b>70 mM pyridazinone 1 in solution</b>						
Component	[Theoretical] mM	Peak Area	# Protons	[Measured] mM	Measured umol	Measured mol%
Pyridazinone <b>1</b>	70	1.07	1	76.0	152.1	100.0
Biphenyl	81	2.28	2			
<b>70 mM Pyridazinone 1 + 70 mM NBS in solution</b>						
Component	[Theoretical] mM	Peak Area	# Protons	[Measured] mM	Measured umol	Measured mol%
Pyridazinone <b>1</b>	70	0.87	1	58.7	117.5	77.0
Succinimide	70	0.26	1	17.6	35.1	23.0
Biphenyl	81	2.40	2			
Total NH				76.3	152.6	

## ESI.10. Analysis of random forest parameter importance modeling

The first analysis was conducted to investigate whether the high variable importance of the additive variable was observed due to its larger number of factor levels compared to other variables. We repeated the RF variable importance calculation 100 times, for both the original and randomly shuffled additive variable. The additive pKa numerical descriptor was excluded due to correlation. The boxplot below shows the comparison between the “%-increase-MSE” variable importance scores between these two settings. When the additive feature was shuffled, the corresponding “%-increase-MSE” reduced significantly compared to the “%-increase-MSE” using the original additive feature. In other words, the additive feature was no longer ranked among the top important features after being shuffled despite the shuffled data having the same number of factor levels in additive.

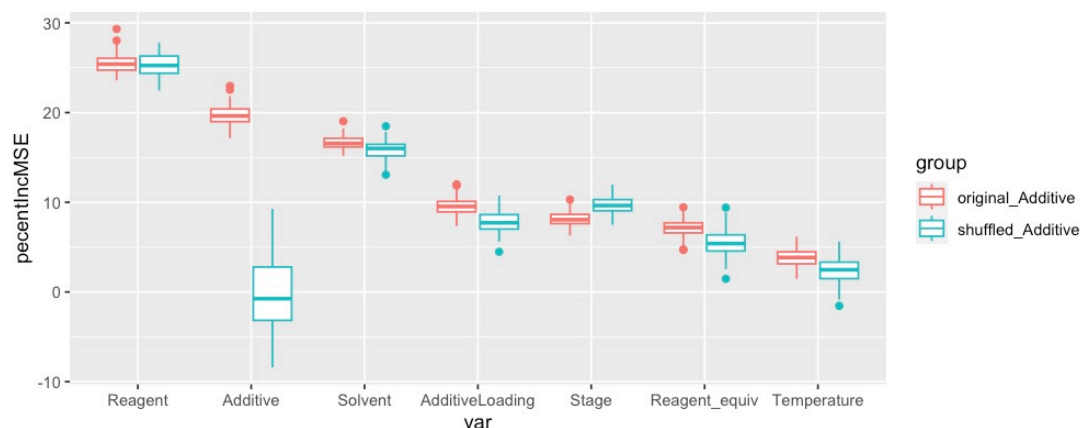
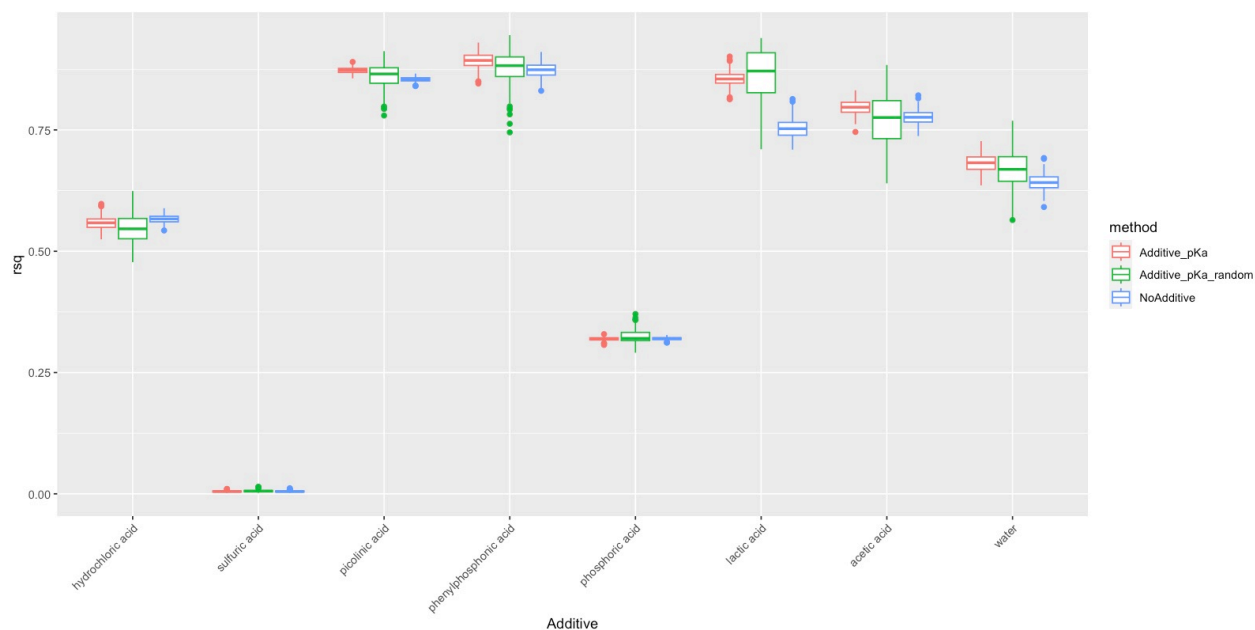


**Figure SI.15.** Analysis of additive parameter importance

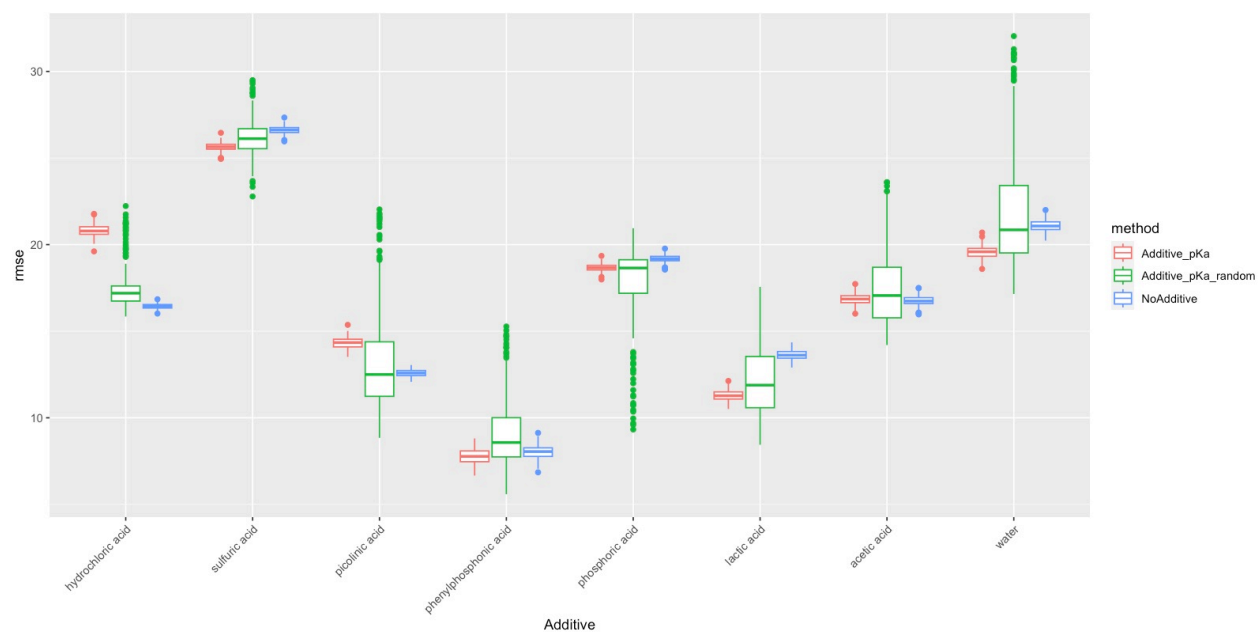
The second analysis was conducted to investigate whether the numerical additive pKa feature helped to improve the model generalizability for unseen additives. We simulated a prospective out-of-sample test set using the existing data by selecting each of the eight additive categories as the test set with an unseen additive. For example, selecting data with “acetic acid” as the test set, while using the rest of data containing the remaining seven additives as the training set. We compared three featurization methods for each train/ test split and repeated with different random seeds 300 times: 1) Original additive pKa variable; 2) Replacing all the additive pKa values with random values generated from a normal distribution with the same mean and

standard deviation; 3) Removing additive pKa. The factor variable additive was excluded from this analysis since it could not be applied to a new additive category. The two boxplots below show the R2 and RMSE on each test set from 300 repeated experiments, and the two summary tables contain the average metrics across repeated experiments. The results suggest that meaningful featurization of additive pKa may help to improve the model generalization performance for some new additives, such as lactic acid, phenylphosphonic acid, and water, compared to random featurization or omitting additive. However, our dataset is obtained from unbalanced optimization campaigns. To further validate any findings or observations from this dataset, it would be necessary to conduct additional experiments with a randomized experimental design and random-control procedures, which is out-of-scope of this work.



method	hydrochloric acid	sulfuric acid	picolinic acid	phenylphosphonic acid	phosphoric acid	lactic acid	acetic acid	water
Additive_pKa	0.558	0.005	0.873	0.892	0.319	0.855	0.796	0.682
Additive_pKa_random	0.547	0.006	0.862	0.878	0.324	0.861	0.772	0.669
NoAdditive	0.566	0.005	0.854	0.873	0.320	0.752	0.776	0.643

**Figure SI.16.** Analysis of additive pKa parameter importance ( $R^2$ )



method	hydrochloric acid	sulfuric acid	picolinic acid	phenylphosphonic acid	phosphoric acid	lactic acid	acetic acid	water
Additive_pKa	20.809	25.647	14.336	7.772	18.663	11.276	16.856	19.579
Additive_pKa_random	17.495	26.129	13.257	9.079	17.816	12.322	17.512	21.943
NoAdditive	16.437	26.619	12.575	8.021	19.193	13.628	16.756	21.094

**Figure SI.17.** Analysis of additive pKa parameter importance (RMSE)

## ESI.11. Experimental

### General

Commercial reagents were purchased from Millipore Sigma, Oakwood, Combi-Blocks, Alfa Aesar, Acros, and Strem, and used as received. Anhydrous solvents were purchased from Millipore Sigma and used as received. Aqueous solutions were deoxygenated through subsurface nitrogen sparge for a minimum of 30 minutes.

Stock solutions were prepared manually in anhydrous solvents under N<sub>2</sub> atmosphere and placed on the robot deck for autonomous execution. A fluoropolymer and metal top-sealed 48-well photoreactor with 1 mL glass vial inserts was equilibrated at the designated reaction temperature under 20 psig of N<sub>2</sub> with 400 rpm agitation. The photoreactor was irradiated with an LED array.

### Equipment

Autonomous optimization experiments were executed using a Chemspeed SWING XL robotic system equipped with a four-needle dispense head and four 1 mL syringe pumps to enable accurate dispenses at low volumes. Agitation was carried out through an integrated custom V&P scientific two-position tumble stirring module and temperature control was achieved through an integrated Huber Unistat chiller with temperature feedback control. Photochemical reactions were executed in a 48 well Analytical Sales Temperature Controlled Reactor (TCR) prototype and irradiated with a modified Analytical Sales Lumidox II LED array. Online HPLC analysis was carried out through an integrated Agilent 1290 UPLC equipped with a photodiode array detector and a custom sampling valve installed on the robot.

Compounds were purified on a CombiFlash purification system employing Redisep Rf Gold silica gel columns. <sup>1</sup>H NMR spectra for characterization were acquired on a Bruker 500 MHz instrument (4 scans). Samples were prepared in DMSO-*d*<sub>6</sub> and spectra were calibrated to the DMSO-*d*<sub>6</sub> reference peak at 2.50 ppm. <sup>13</sup>C NMR spectra for characterization were recorded on a Bruker 500 MHz instrument (5120 scans). Samples were prepared in DMSO-*d*<sub>6</sub> and spectra were calibrated to the DMSO-*d*<sub>6</sub> reference peak at 40 ppm. ESI+ MS for characterization were acquired on an Agilent 1290 UPLC-MS.

### **Representative procedure for high throughput reaction profiling experiments**

The described procedure was executed in batch for 48 - 96 reactions. To each well was dispensed 200  $\mu\text{l}$  of a mixture of starting material **1** (63.0  $\mu\text{mol}$ , 0.315 M), brominating reagent (75.6  $\mu\text{mol}$ , 0.378 M), and octofluorotoluene (6.3  $\mu\text{mol}$ , 0.032 M). This was followed by the addition of acid additive (6.3  $\mu\text{mol}$ , 50  $\mu\text{l}$  of 0.126 M stock solution). The reaction mixture was irradiated with a 405 or 470 nm LED array for the designated time interval at 25 °C. The LED array was switched off and 10  $\mu\text{l}$  of each reaction mixture was transferred to a 96-well polypropylene collection block prefilled with 800  $\mu\text{l}$  of ACN diluent. The irradiation-sampling sequence was continued until between 6 and 12 samples were aliquoted and diluted from each reaction mixture. The diluted samples were subjected to offline UPLC analysis.

### **Representative procedure for LED NMR experiments**

To a 2 mL volumetric flask under  $\text{N}_2$  atmosphere was dispensed stock solutions of 6-methyl-4-(trifluoromethyl)pyridazin-3(2H)-one **1** (25.0 mg, 0.140 mmol) and NBS (30.3 mg, 0.168 mmol) in  $\text{ACN-}d_3$ . This was followed by the addition of a stock solution of  $\text{H}_3\text{PO}_4$  (1.39 mg, 0.0140 mmol) in  $\text{ACN-}d_3$ . The resulting mixture was adjusted to 2 mL of volume with  $\text{ACN-}d_3$  and 600  $\mu\text{l}$  was transferred to a 5 mm thin wall NMR tube followed by the placement of the coaxial insert. The joint was parafilm and the sample was wrapped with foil to keep out the light. The sample was irradiated at 445 nm at the desired temperature under LED NMR acquisition.

### **Representative procedure for autonomous reproducibility experiments**

The described procedure was executed sequentially for each reaction. To each well was dispensed methyl pyridazinone **1** (20  $\mu\text{mol}$ , 80  $\mu\text{l}$  of 0.25 M stock solution), NBS (25  $\mu\text{mol}$ , 100  $\mu\text{l}$  of 0.25 M stock solution),  $\text{H}_2\text{SO}_4$  (2  $\mu\text{mol}$ , 20  $\mu\text{l}$  of 0.10 M stock solution), and anhydrous ACN or DMC (50  $\mu\text{l}$ ) to ensure a total reaction volume of 250  $\mu\text{l}$ . The reaction mixture was irradiated with an LED array for two minutes at 25 °C. The LED array was switched off and 5  $\mu\text{l}$  of the reaction mixture was transferred to a 96-well polypropylene collection block prefilled with 400  $\mu\text{l}$  of ACN diluent. Upon needle-mixing, 40  $\mu\text{l}$  of diluted sample from the collection block was aliquoted and injected to the on-deck sampling valve outfitted with a 2  $\mu\text{l}$  loop. The valve was automatically switched to transfer the sample to the UPLC for analysis. The irradiation-sampling-online analysis sequence was continued until the reaction reached a plateau or a maximum number of 12 samples were analyzed.

### Procedure for scale-up experiment in flow

To a 50 mL volumetric flask was added 6-methyl-4-(trifluoromethyl)pyridazin-3(2H)-one **1** (12.5 mmol, 2.23 g) and NBS (15.0 mmol, 2.67 g), followed by 25 mL of ACN to dissolve all solids. H<sub>2</sub>SO<sub>4</sub> (1.25 mmol, 0.0668 mL) was added and the volume adjusted to 50 mL with ACN. The solution was flowed through a Vaportec system equipped with a 3 mL reactor under 450 nm irradiation at 0.5 ml/min (6 min residence time). After 25 min, the product stream collection was initiated and continued for 65 min. 32.6 ml was collected to generate 6-(bromomethyl)-4-(trifluoromethyl)pyridazin-3(2H)-one **2** in 69% assay yield and 6-(dibromomethyl)-4-(trifluoromethyl)pyridazin-3(2H)-one **3** in 13% assay yield, with 5% assay yield 6-methyl-4-(trifluoromethyl)pyridazin-3(2H)-one **1** remaining.

### Representative procedure for autonomous optimization reactions

The described procedure was executed sequentially for each reaction. To each well was dispensed starting material **1** (20 μmol, 80 μl of 0.25 M stock solution), brominating reagent (20 - 30 μmol, 80 - 120 μl of 0.25 M stock solution), acid additive (0.2 – 5.0 μmol, 2 - 50 μl of 0.10 M stock solution), and anhydrous ACN or DMC (100 - 188 μl) to ensure a total reaction volume of 350 μl. The reaction mixture was irradiated with an LED array for two minutes at a designated reaction temperature between 5 and 35 °C. The LED array was switched off and 5 μl of the reaction mixture was transferred to a 96-well polypropylene collection block prefilled with 400 μl of ACN diluent. Upon needle-mixing, 40 ul of diluted sample from the collection block was aliquoted and injected to the on-deck sampling valve outfitted with a 2 μl loop. The valve was automatically switched to transfer the sample to the UPLC for analysis (Figure SI.13). The irradiation-sampling-online analysis sequence was continued until the reaction reached a plateau or a maximum number of 12 samples were analyzed.

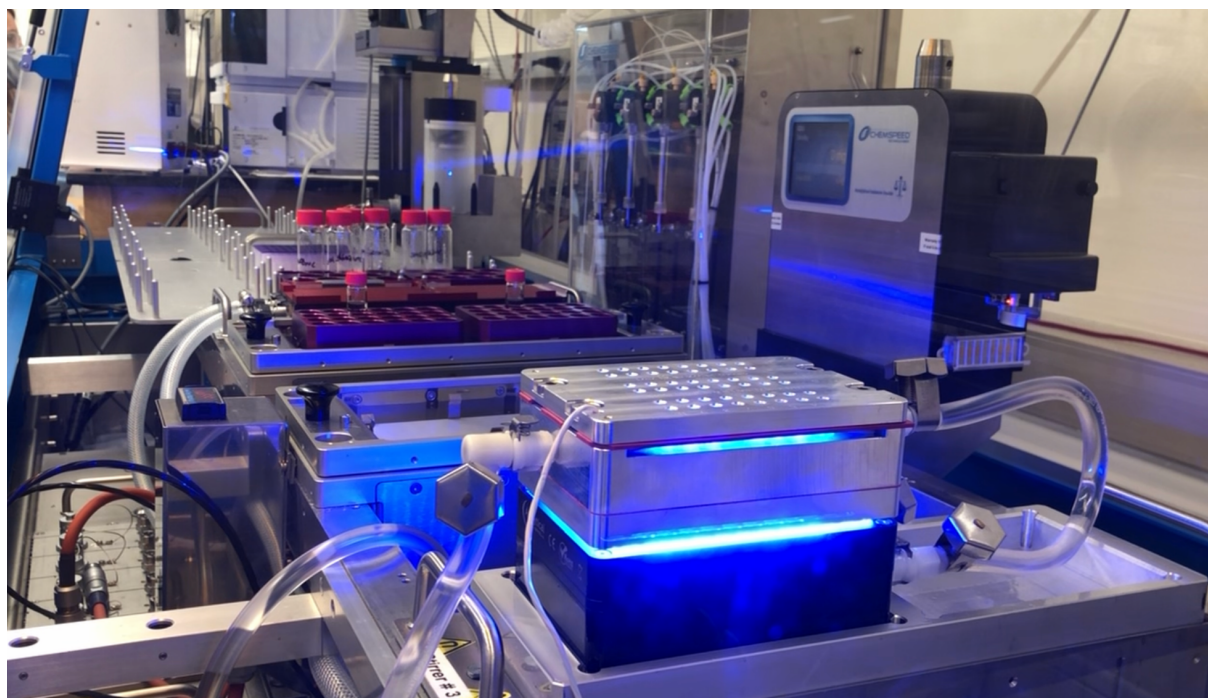
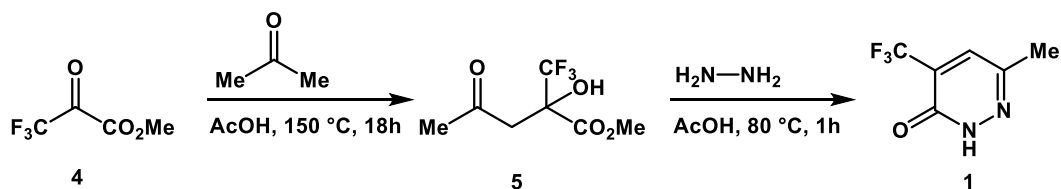


**Figure SI.18.** Image of the Chemspeed SWING XL deck for autonomous experimentation

**Procedure for the synthesis of 6-methyl-4-(trifluoromethyl)pyridazin-3(2H)-one 1:**



To a 1 L flask was added acetone (1.92 mol, 112 g, 141 ml) and AcOH (400 mL). Methyl 3,3,3-trifluoro-2-oxopropanoate **4** (1.28 mol, 200 g, 145 ml) was charged via addition funnel over 2 min, raising the temperature rose to 46 °C. The resulting mixture was flowed through a 5 ml flow reactor housed in a 150 °C oven until steady state was established at 0.416 ml/min and the reactor output was collected for 18 h 30 min to yield 519 g of solution containing 192 g (0.897 mol) of methyl 2-hydroxy-4-oxo-2-(trifluoromethyl)pentanoate **5**.

To a 3 L round bottom flask was transferred 290 g of solution containing 107 g (0.500 mol) of methyl 2-hydroxy-4-oxo-2-(trifluoromethyl)pentanoate **5**. To this solution was charged hydrazine hydrate (0.752 mol, 37.6 g, 36.5 ml) under N<sub>2</sub> atmosphere over 10 min, raising the temperature to 50 °C. The reaction was aged at 80 °C for 1 h. The reaction was cooled to 25 °C and 322 ml of water was added via addition funnel over 20 min. This was followed by the

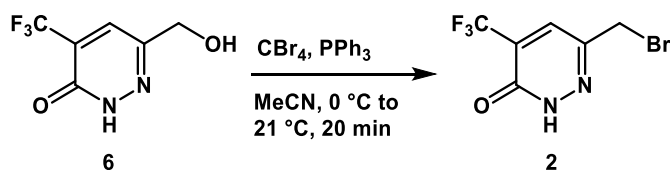
addition of 644 ml 35 wt% NaH<sub>2</sub>PO<sub>4</sub> via addition funnel over 40 min. The mixture was cooled to 0 °C, filtered and the cake washed twice with 160 ml water. The wet cake was dried in a vacuum oven under N<sub>2</sub> sweep to yield 77.3 g of 6-methyl-4-(trifluoromethyl)pyridazin-3(2H)-one **1** in 87% yield.

<sup>1</sup>H NMR (500 MHz, DMSO-*d*<sub>6</sub>) δ 13.39 (s, 1H), 7.86 – 7.83 (m, 1H), 2.31 (s, 3H).

<sup>13</sup>C NMR (126 MHz, DMSO-*d*<sub>6</sub>) δ 156.42, 144.42, 133.99 – 133.63 (m), 127.35 (q, *J* = 31.0 Hz), 122.09 (q, *J* = 272.7 Hz), 20.52.

MS ESI+: (m/z calc. for C<sub>6</sub>H<sub>5</sub>F<sub>3</sub>N<sub>2</sub>O, [M + H] = 179.0); found = 179.0.

#### Procedure for the synthesis of 6-(bromomethyl)-4-(trifluoromethyl)pyridazin-3(2H)-one **2**:



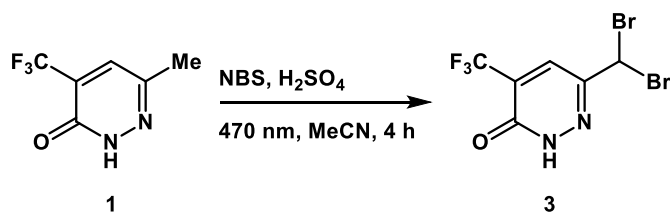
To a 100 mL round bottom flask was added 6-(hydroxymethyl)-4-(trifluoromethyl)pyridazin-3(2H)-one **6** (25.8 mmol, 5.00 g), CBr<sub>4</sub> (38.6 mmol, 12.8 g) and ACN (50 ml). The mixture was cooled in an ice batch and PPh<sub>3</sub> (28.3 mmol, 7.42 g) was added, raising the temperature to 21 °C. The mixture was concentrated to dryness and purified over silica gel to yield 6-(bromomethyl)-4-(trifluoromethyl)pyridazin-3(2H)-one **2** (the yield was not determined).

<sup>1</sup>H NMR (500 MHz, DMSO-*d*<sub>6</sub>) δ 13.78 (s, 1H), 8.09 – 8.05 (m, 1H), 4.62 (s, 2H).

<sup>13</sup>C NMR (126 MHz, DMSO-*d*<sub>6</sub>) δ 156.26, 143.97, 133.10 (q, *J* = 4.9 Hz), 128.16 (q, *J* = 31.5 Hz), 121.80 (q, *J* = 272.9 Hz), 31.40.

MS ESI+: (m/z calc. for C<sub>6</sub>H<sub>4</sub>BrF<sub>3</sub>N<sub>2</sub>O, [M + H] = 256.9); found = 256.9.

#### Procedure for the synthesis of 6-(dibromomethyl)-4-(trifluoromethyl)pyridazin-3(2H)-one **3**:



To a 40 ml vial was charged 6-methyl-4-(trifluoromethyl)pyridazin-3(2H)-one **1** (22.5 mmol, 4.00 g), NBS (56.1 mmol, 10.0 g) and ACN (40 ml). This was followed by the addition of H<sub>2</sub>SO<sub>4</sub> (2.25 mmol, 0.220 g, 0.120 ml). The mixture was split into 2 vials and irradiated with a Penn PhD photoreactor at 470 nm for 4 h. The mixture was concentrated to dryness and purified over silica gel to yield 5.56 g of 6-(dibromomethyl)-4-(trifluoromethyl)pyridazin-3(2H)-one **3** in 82% yield.

<sup>1</sup>H NMR (500 MHz, DMSO-*d*<sub>6</sub>) δ 13.92 (s, 1H), 8.15 – 8.11 (m, 1H), 7.25 (s, 1H).

<sup>13</sup>C NMR (126 MHz, DMSO-*d*<sub>6</sub>) δ 156.12, 144.94, 130.57 (q, *J* = 4.9 Hz), 128.76 (q, *J* = 31.8 Hz), 121.52 (q, *J* = 273.1 Hz), 38.27.

MS ESI+: (m/z calc. for C<sub>6</sub>H<sub>3</sub>Br<sub>2</sub>F<sub>3</sub>N<sub>2</sub>O, [M + H] = 334.9); found = 334.9.

## ESI.12. Characterization data

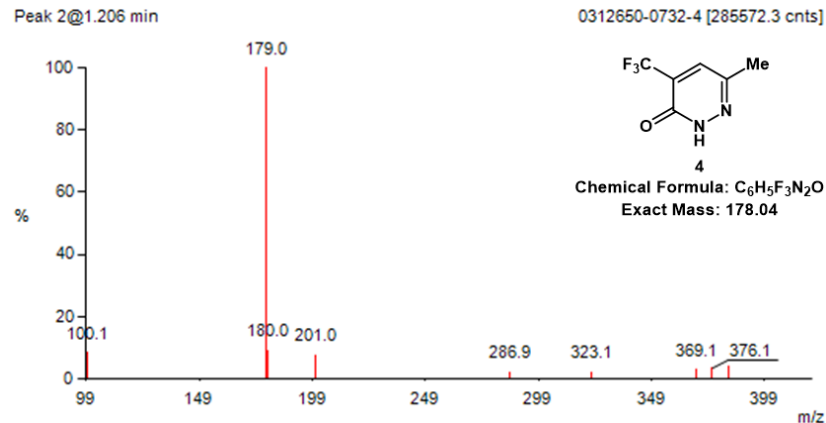


Figure SI.19. MS ESI+ of 1

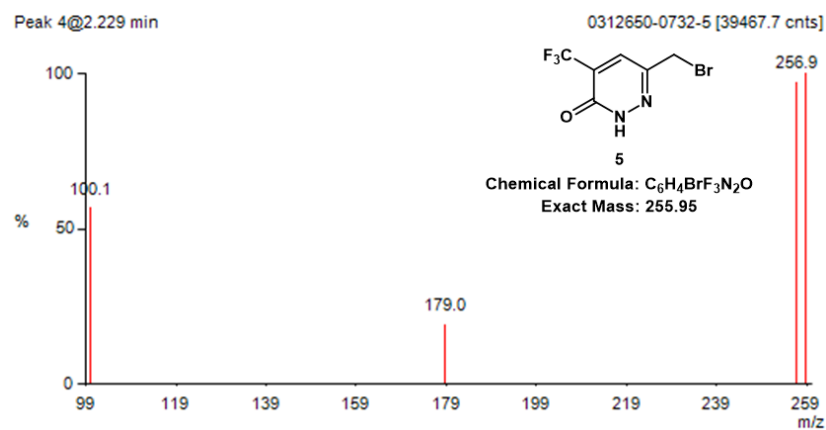


Figure SI.20. MS ESI+ of 2

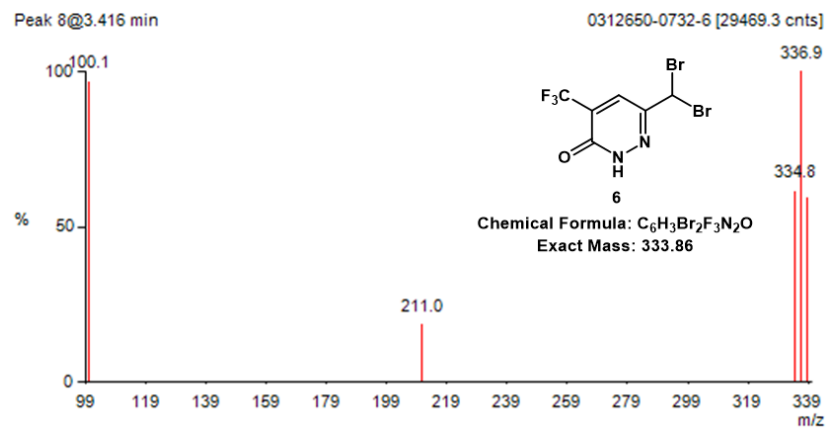


Figure SI.21. MS ESI+ of 3

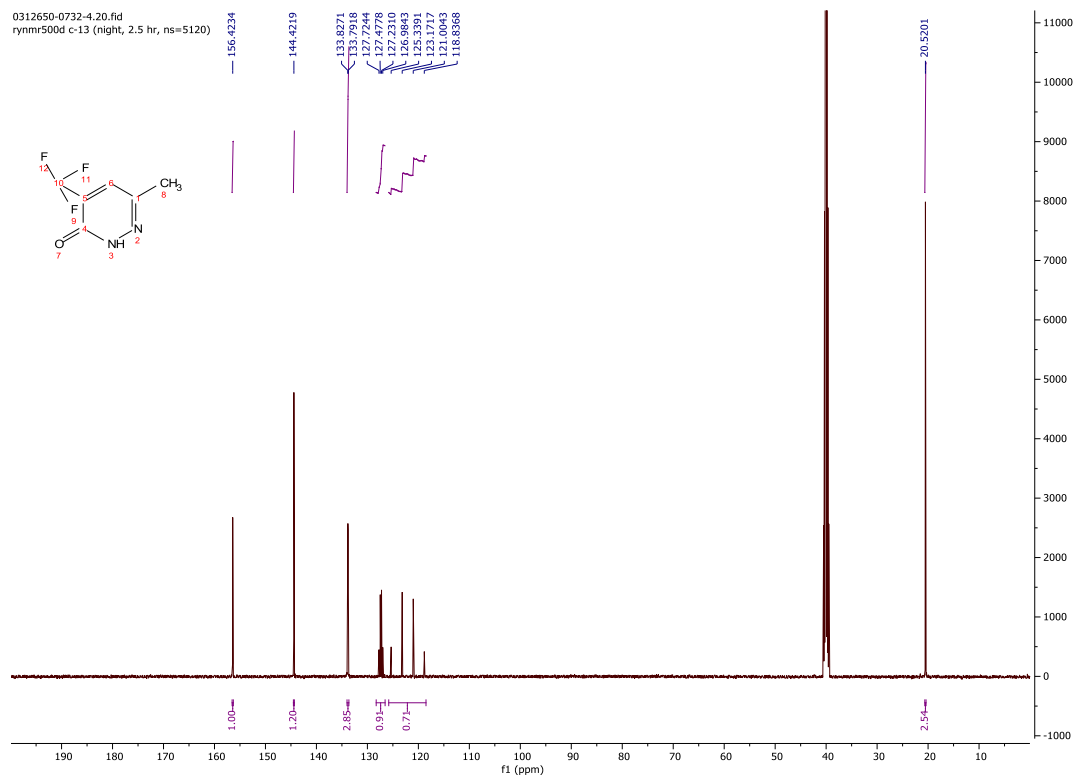
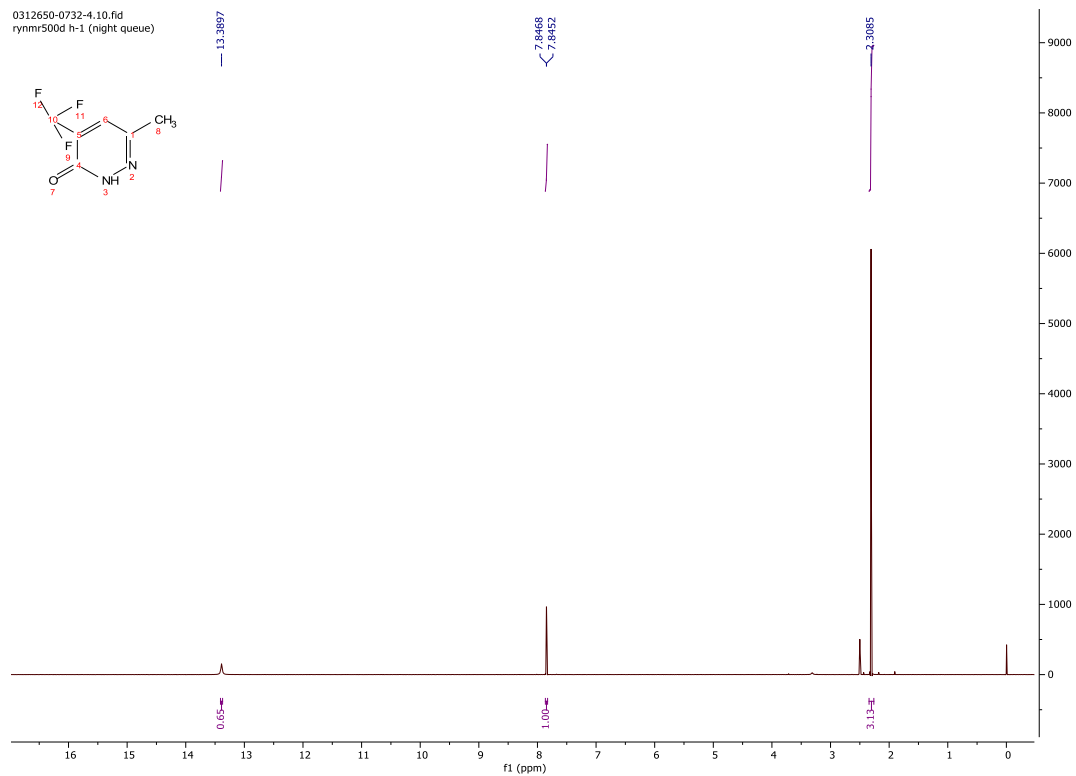


Figure SI.22.  $^1\text{H}$  and  $^{13}\text{C}$  NMR spectra of **1** in  $\text{DMSO-}d_6$

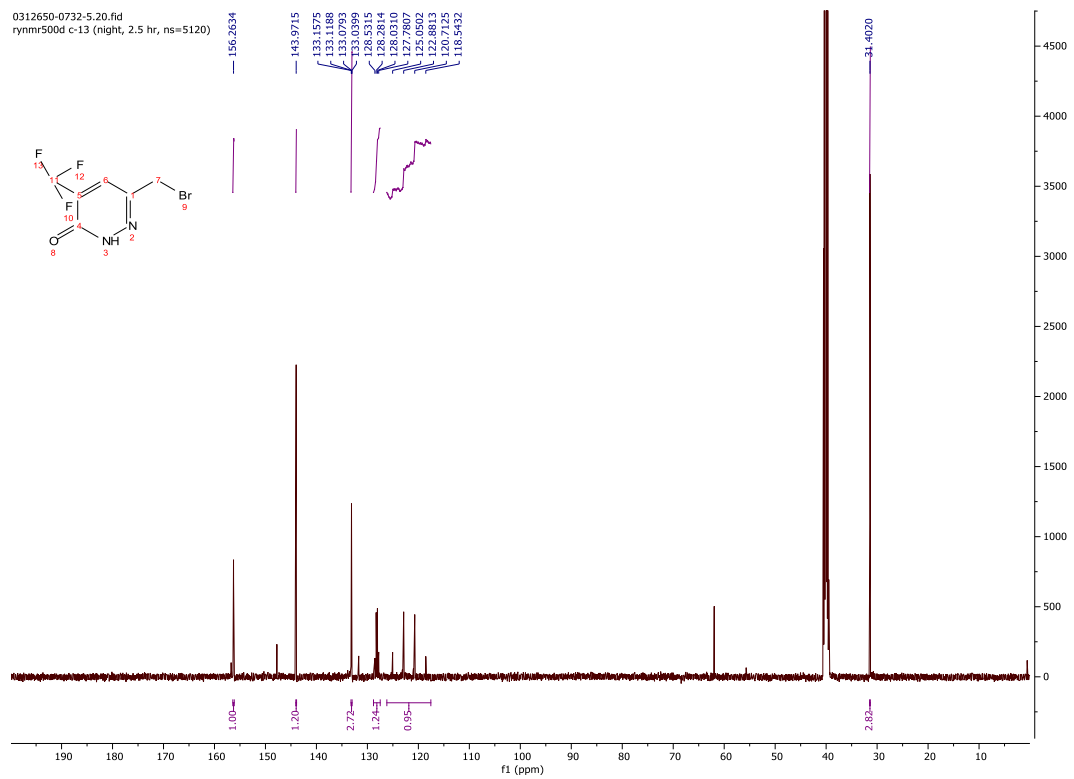
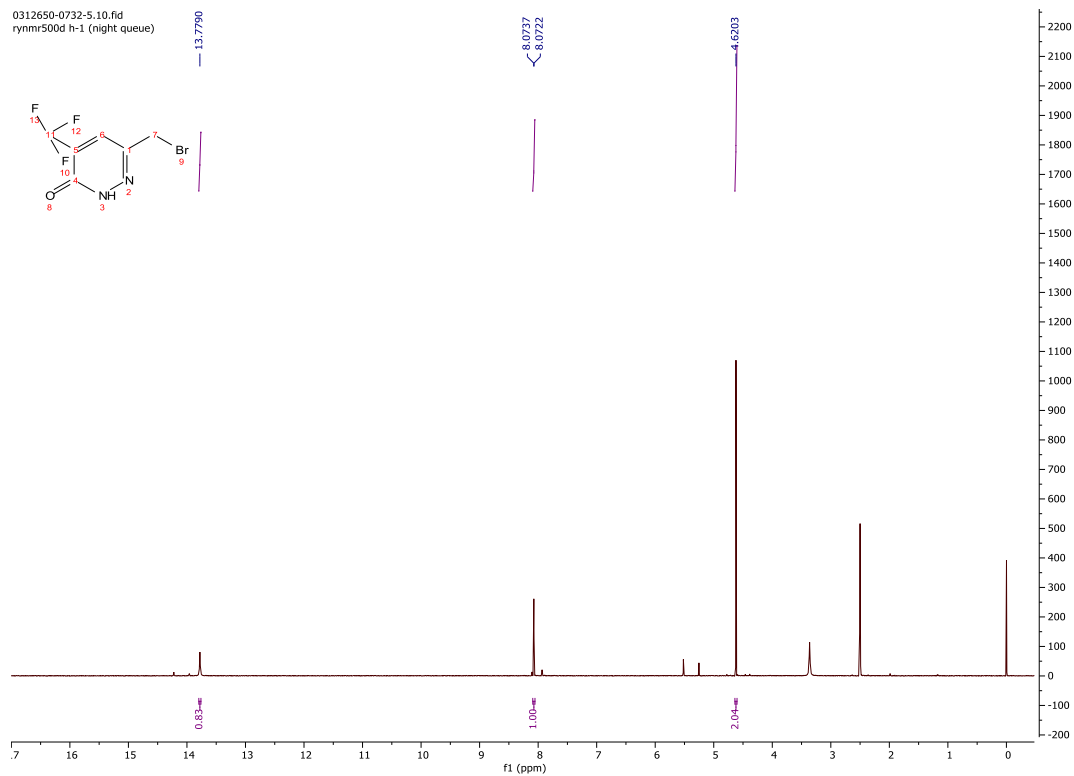


Figure SI.23.  $^1\text{H}$  and  $^{13}\text{C}$  NMR spectra of **2** in  $\text{DMSO-}d_6$

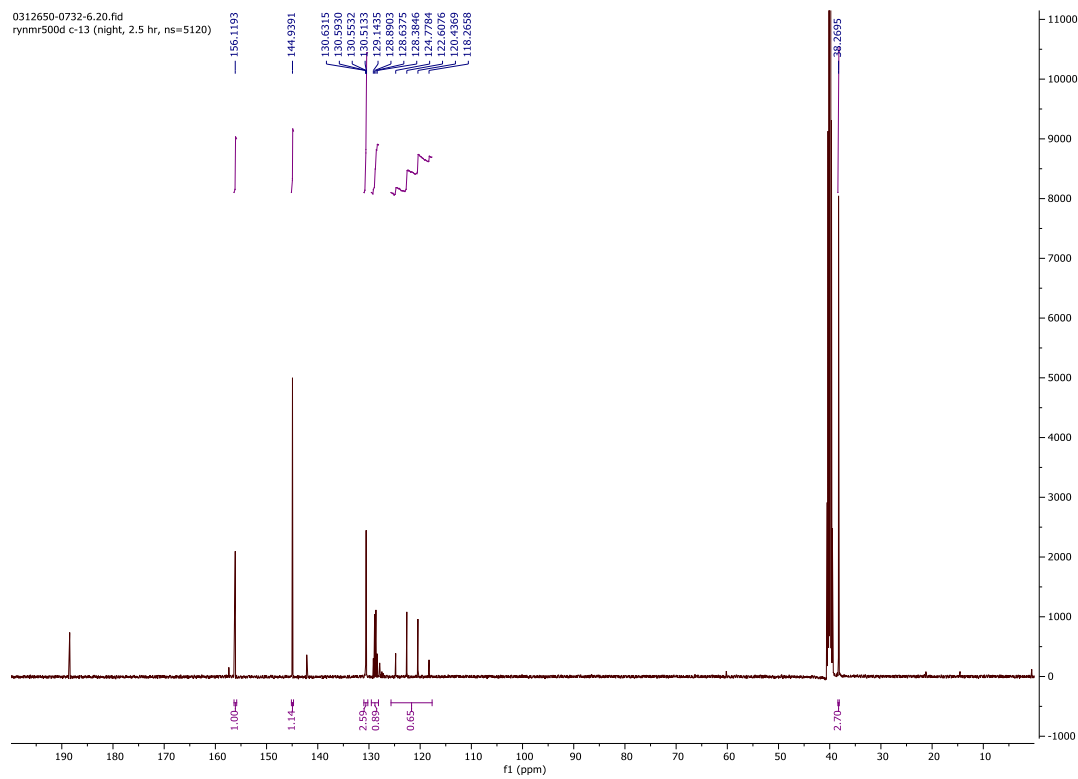
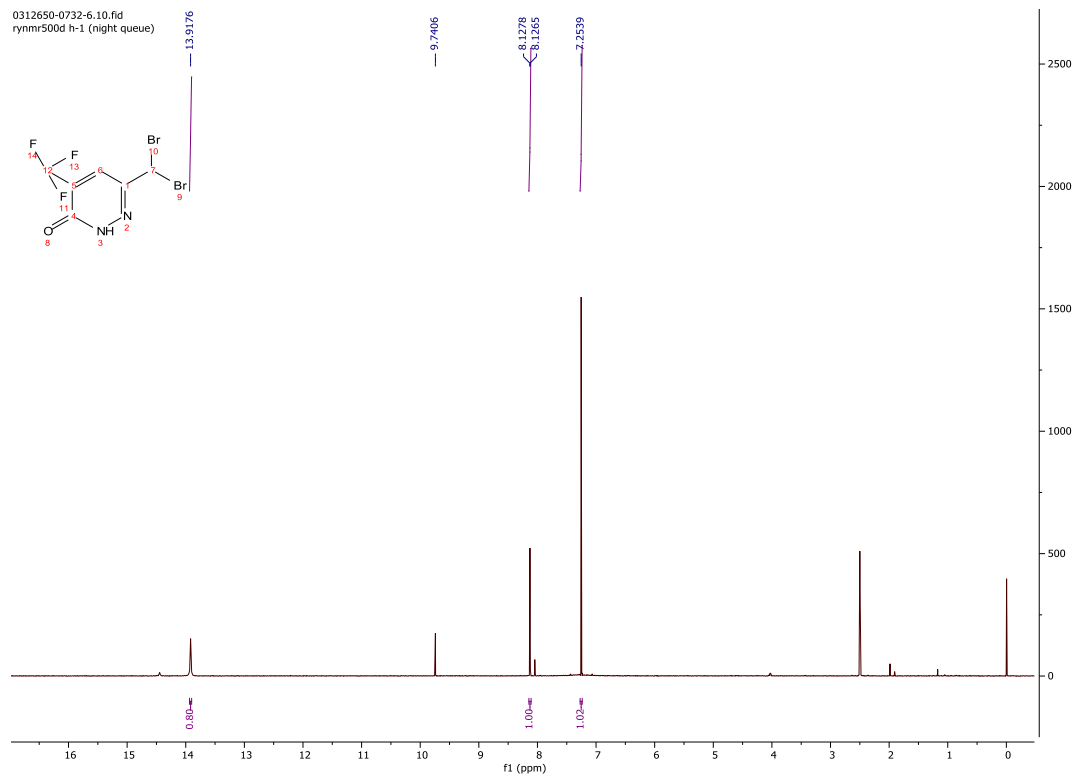


Figure SI.24.  $^1\text{H}$  and  $^{13}\text{C}$  NMR spectra of **3** in  $\text{DMSO-}d_6$

### ESI.13. Analytical methods

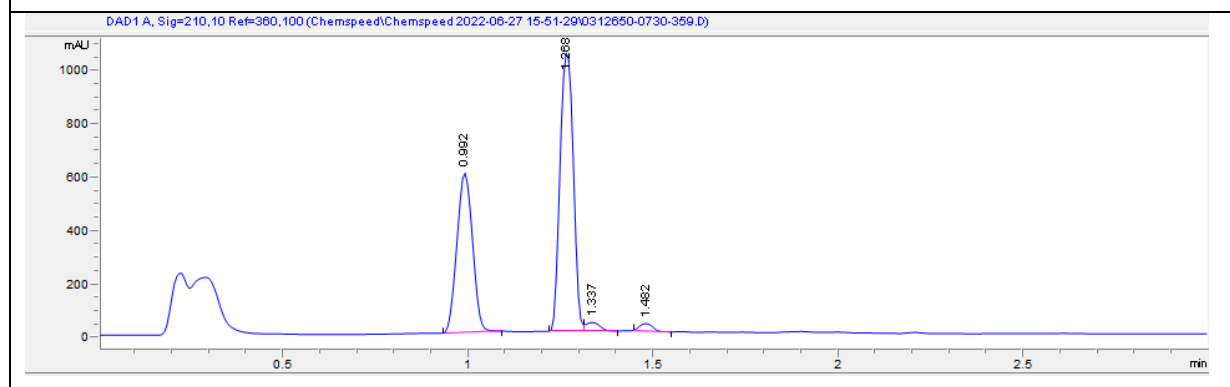
Reaction analyses were carried out using an Agilent 1100 HPLC-UV using the method below:

**Table SI.3.** HPLC-UV method for optimization sample analysis

Column:	Agilent Poroshell 210 PFP 2.7 $\mu$ m, 4.6 x 50 mm	
Column Temperature:	50 °C	
Flow Rate:	0.85 ml/min	
Detection:	210 nm	
Acquisition Time:	3.0 min	
Mobile Phase:	Solvent A = 2 mM ammonium formate in water; Solvent B = 2 mM ammonium formate in acetonitrile 10% water	
Mobile Phase Program:	Time	B%
	0.0 min	5
	1.5 min	100
	2.5 min	100
	3.0 min	5
Injection Volume:	2 $\mu$ L	

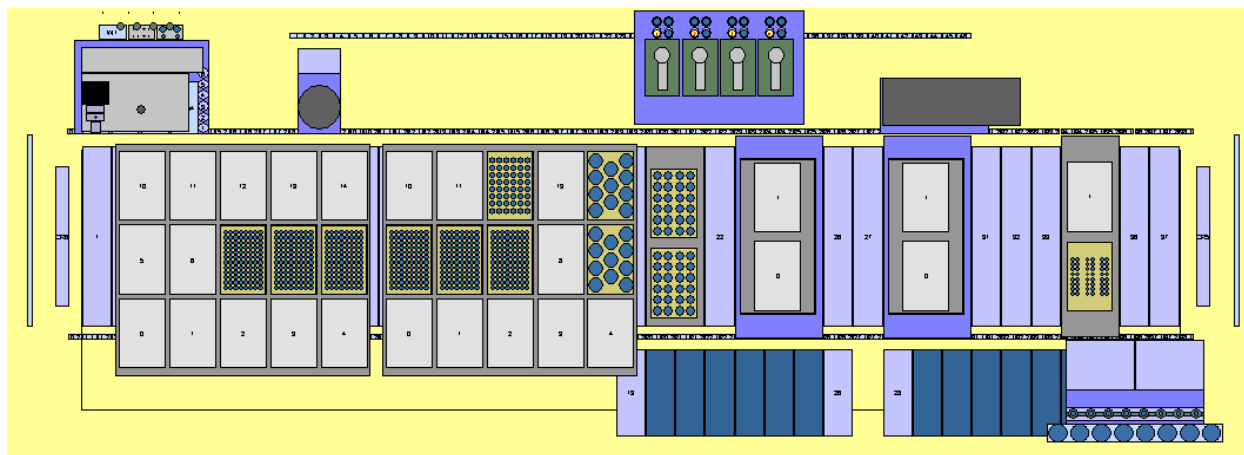
Compound Name:	Retention time:
6-methyl-4-(trifluoromethyl)pyridazin-3(2H)-one <b>1</b>	0.99 min
6-(bromomethyl)-4-(trifluoromethyl)pyridazin-3(2H)-one <b>2</b>	1.27 min
6-(dibromomethyl)-4-(trifluoromethyl)pyridazin-3(2H)-one <b>3</b>	1.48 min

Example Chromatogram



## ESI.14. Chemspeed protocol

Below is an excerpt of the Chemspeed protocol used in autonomous optimization.



Task	Name	Parameter	Description
1	Prime Lines	Execute 'Cycles' times (counter 'loop')	Prime Lines
	Transfer Volumetrically	Transfer liquid from variable 'Reservoir_solvent' to variable 'Rinse_station' with Needle	
	<insert sub tasks here>		
2	Autonomous Process Optim	Execute Once	
1	Show Dialog	OK-Dialog: 'Please start hplc sequence, then code'	
2	Transfer Volumetrically	Transfer liquid from valve ports E to Injection valve 1 Load with Needle Head #1	
3	Wait	Waiting for 2 seconds	
4	Execute Operation	Switch HPLC On #1: Set State	
5	Wait	Waiting for 2 seconds	
6	Execute Operation	Switch HPLC On #1: Set State	
7	Transfer Volumetrically	Transfer liquid from valve ports E to Injection valve 1 Inject with Needle Head #1	
8	Variables	Execute Once	Create variables
1	Loop	Execute Once	Hold for csv update
1	CSV Import	Execute While 'Experiment_ID <> Experiment_count'	
1	Wait	Waiting for 5 seconds	
2	Import CSV	import row 'Experiment_count' from file 'Closed Loop APO.csv'.	
	<insert sub tasks here>		
2	Heat / Cool	Thermostat ON on zone Reactions	
3	Log Data	Log "Experiment_ID=' + Experiment_ID + ' ; Experiment_count=' + Experiment_count	
4	SM	Execute Once	Dispense SM
1	Transfer Volumetrically	Transfer liquid from SM_MeCN to variable 'One_Reaction' with Needle Head #1	
2	Transfer Volumetrically	Transfer liquid from SM_DMC to variable 'One_Reaction' with Needle Head #1	
	<insert sub tasks here>		
5	Reagent	Execute Once	Dispense Reagents
1	Transfer Volumetrically	Transfer liquid from NBS_MeCN to variable 'One_Reaction' with Needle Head #1	
2	Transfer Volumetrically	Transfer liquid from NBS_DMC to variable 'One_Reaction' with Needle Head #1	
3	Transfer Volumetrically	Transfer liquid from DBDMH_MeCN to variable 'One_Reaction' with Needle Head #1	
4	Transfer Volumetrically	Transfer liquid from DBDMH_DMC to variable 'One_Reaction' with Needle Head #1	
5	Prime Lines	Execute 'Cycles' times (counter 'loop')	Prime Lines
1	Transfer Volumetrically	Transfer liquid from variable 'Reservoir_solvent' to variable 'Rinse_station' with Needle	
	<insert sub tasks here>		
	<insert sub tasks here>		
6	Additive	Execute Once	Dispense Additives
1	Transfer Volumetrically	Transfer liquid from 1_HCl_MeCN to variable 'One_Reaction' with Needle Head #1	
2	Transfer Volumetrically	Transfer liquid from 2_H2SO4_MeCN to variable 'One_Reaction' with Needle Head #1	
3	Transfer Volumetrically	Transfer liquid from 3_Picolinic_MeCN to variable 'One_Reaction' with Needle Head #	
4	Transfer Volumetrically	Transfer liquid from 4_Phenylphosphonic_MeCN to variable 'One_Reaction' with Nee	

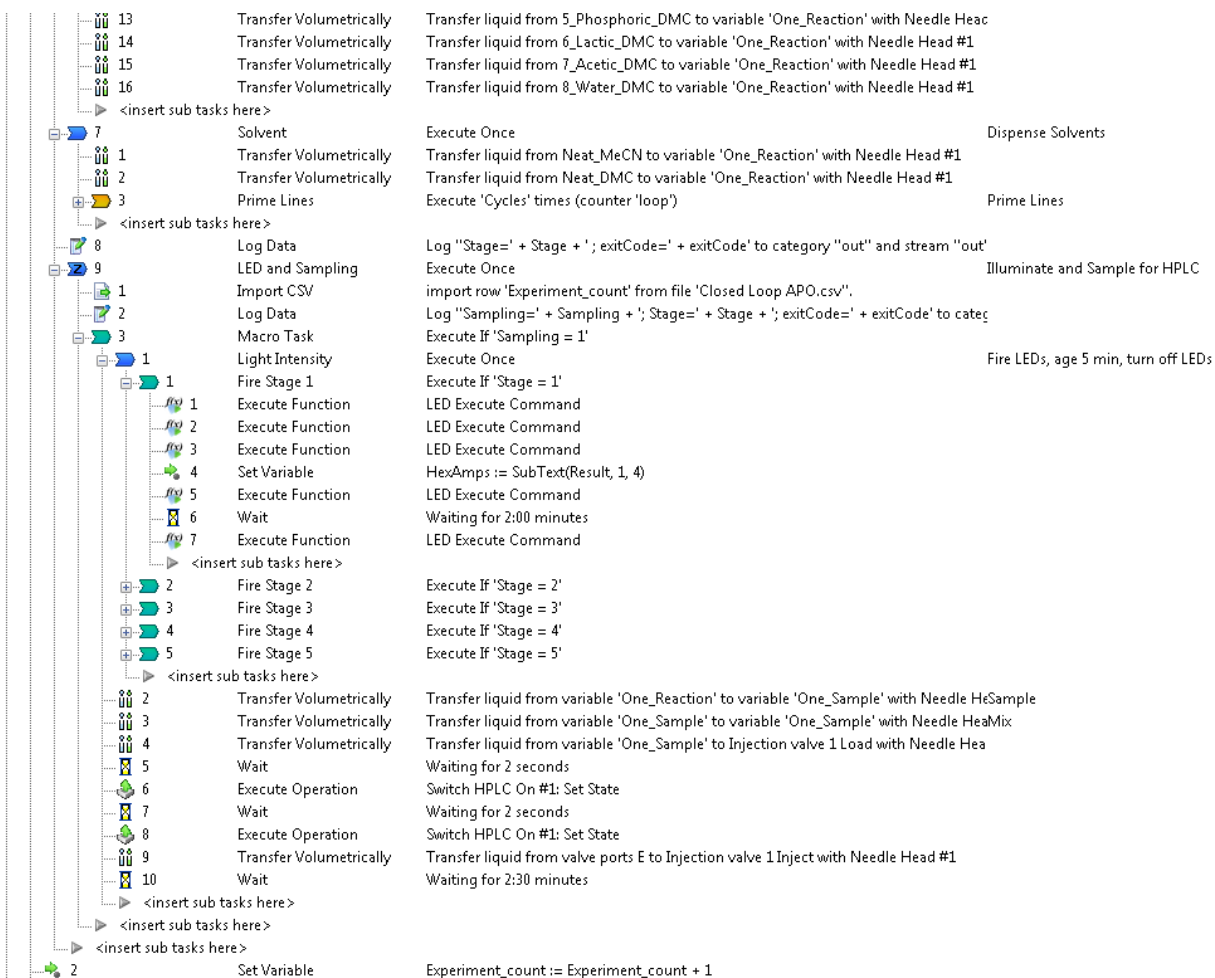


**Figure SI.25.** Chemspeed protocol for autonomous optimization of the photobromination reaction

## ESI References

- 1 C. C. Le, M. K. Wismer, Z. C. Shi, R. Zhang, D. V. Conway, G. Li, P. Vachal, I. W. Davies and D. W. C. MacMillan, *ACS Cent. Sci.*, 2017, **3**, 647–653.
- 2 T. D. Svejstrup, A. Chatterjee, D. Schekin, T. Wagner, J. Zach, M. J. Johansson, G. Bergonzini and B. König, *ChemPhotoChem*, 2021, **5**, 808–814.
- 3 Lumidox LED Arrays, <https://www.analytical-sales.com/product-category/photoredox-parallel-synthesis/lumidox-led-arrays-lamps/>.
- 4 D. A. DiRocco, K. Dykstra, S. Krska, P. Vachal, D. V. Conway and M. Tudge, *Angew. Chemie Int. Ed.*, 2014, **53**, 4802–4806.
- 5 J. Twilton, M. Christensen, D. A. DiRocco, R. T. Ruck, I. W. Davies and D. W. C. MacMillan, *Angew. Chemie - Int. Ed.*, 2018, **57**, 5369–5373.
- 6 F. Hutter, H. H. Hoos and K. Leyton-Brown, in *Learning and Intelligent Optimization*, Springer, 2011, pp. 507–523.
- 7 scikit-learn, <https://scikit-learn.org/stable/>.
- 8 P. F. de Aguiar, B. Bourguignon, M. S. Khots, D. L. Massart and R. Phan-Thau-Luu, *Chemom. Intell. Lab. Syst.*, 1995, **30**, 199–210.
- 9 J. P. Reid, R. S. J. Proctor, M. S. Sigman and R. J. Phipps, *J. Am. Chem. Soc.*, 2019, **141**, 19178–19185.
- 10 B. Shahriari, K. Swersky, Z. Wang, R. P. Adams and N. De Freitas, *Proc. IEEE*, 2016, **104**, 148–175.
- 11 P. I. Frazier, *A Tutorial on Bayesian Optimization*, 2018.

- 12 E. B. Corcoran, J. P. McMullen, F. Lévesque, M. K. Wismer and J. R. Naber, *Angew. Chemie Int. Ed.*, 2020, **59**, 11964–11968.
- 13 A. Johnston, R. Bhardwaj-Miglani, R. Gurung, A. D. Vassileiou, A. J. Florence and B. F. Johnston, *J. Chem. Inf. Model.*, 2017, **57**, 1807–1815.